AUV Observations of Langmuir Turbulence in a Stratified Shelf Sea

Alexander W. Fisher,[1,2] Nicholas J. Nidzieko,[3]

[1] *Applied Physics Laboratory, University of Washington, Seattle, WA, USA*

[2] *Washington State Department of Ecology, Lacy, Washington, USA*

[3] *Department of Geography, University of California, Santa Barbara, Santa Barbara, CA, USA*

Corresponding author: A.W. Fisher, afisher@apl.washington.edu

Early Online Release: This preliminary version has been accepted for publication in *Journal of Physical Oceanography*, may be fully cited, and has been assigned DOI 10.1175/JPO-D-23-0136.1. The final typeset copyedited article will replace the EOR at the above DOI when it is published.

ABSTRACT: Measurements collected by a REMUS 600 AUV off the coast of southern California demonstrate large-scale coherent wave-driven vortices, consistent with Langmuir turbulence (LT), played a dominant role in structuring turbulent dissipation within the oceanic surface boundary layer. During a 10-hour period with sustained wind speeds of 10 m s^{-1}, Langmuir circulations were limited to the upper third of the surface mixed layer by persistent stratification within the water column. The ensemble-averaged circulation, calculated using conditional averaging of AD2CP velocity profiles using elevated backscattering intensity associated with subsurface bubble clouds, indicates that LT vortex pairs were characterized by an energetic downwelling zone flanked by broader, weaker upwelling regions with vertical velocity magnitudes similar to previous numerical studies of LT. Horizontally-distributed microstructure estimates of turbulent kinetic energy dissipation rates were lognormally-distributed near the surface in the wave mixing layer with the majority of values falling between wall layer scaling and wave transport layer scaling. Partitioning dissipation rates between downwelling centers and ambient conditions suggests that LT may play a dominant role in elevating dissipation rates in the OSBL by redistributing wave breaking turbulence.

Accepted for publication in *Journal of Physical Oceanography*. DOI 10.1175/JPO-D-23-0136.1.

1. Introduction

Turbulence dynamics in the upper ocean control the exchange of mechanical energy, momentum, heat, and gases across the air-sea interface and can dramatically affect the processes through which transport from the surface to depth occurs. Wind acts to generate turbulence directly through wind stress acting on the ocean surface and indirectly through the generation of surface gravity waves. The presence of waves fundamentally alters turbulence in the OSBL relative to classical wall shear layers resulting in turbulent dissipation rates (ε) that typically exceed wall layer scaling, $\varepsilon \propto u_*^3/z$, by up to two orders of magnitude (Agrawal et al. 1992; Drennan et al. 1996; Gerbi et al. 2009; Gemmrich 2010; Sutherland and Melville 2015; Thomson et al. 2016).

The turbulent kinetic energy budget (TKE) for a horizontally homogeneous flow at steady state that includes wave effects can be written as (Kitaigorodskii 1983; McWilliams et al. 1997):

$$-\overline{u_i'w'}\frac{\partial U_i}{\partial z} - \overline{u_i'w'}\frac{\partial U_{Si}}{\partial z} + \frac{g}{\rho_0}\overline{\rho'w'} - \frac{\partial}{\partial z}\left(\frac{1}{2}\overline{u_i'^2w'} + \frac{1}{\rho_0}\overline{p'w'}\right) = \varepsilon \tag{1}$$

where primes denote turbulent fluctuations of velocity ($u = u_1'$, $v = u_2'$, $w = u_3'$), pressure (p'), and density (ρ') and overbars denote time-averaging. The coordinate system is defined such that x_1 and x_2 are horizontal and $x_3 = z$ is positive upward with $z = 0$ at the mean free surface. Capitalized variables indicate the Eulerian horizontal velocity (U_i) and Stokes drift velocity (U_{Si}). The reference density of seawater is denoted as ρ_0 and gravitational acceleration as g. The first two terms on the l.h.s. of equation 1 are the Eulerian shear production and Stokes drift production, respectively. The third term on the l.h.s. is the buoyancy flux and the fourth term on the l.h.s. is the vertical divergence in total TKE transport, which is the sum of the turbulent TKE fluxes driven by turbulent velocity (e.g. turbulent TKE flux) and pressure (e.g. pressure work) fluctuations.

Within a shallow wave transport layer just below the surface, the TKE dissipation rate is balanced by a divergence in total TKE transport (Terray et al. 1996; Scully et al. 2016), such that dissipation rates have been shown to scale as a power law decay (Terray et al. 1996):

$$\frac{\varepsilon H_s}{F_0} = A\left(\frac{z}{H_s}\right)^{\lambda} \tag{2}$$

Accepted for publication in *Journal of Physical Oceanography*. DOI 10.1175/JPO-D-23-0136.1.

where H_s is the significant wave height of the wind sea (Gerbi et al. 2009), F_0 is the surface TKE flux generated by wave energy dissipation via breaking, and A and λ are constants. A lack of consensus regarding the exact value of λ persists, but prior work has generally reported values between $-2 < \lambda < -1$ (Drennan et al. 1996; Gerbi et al. 2009; Gemmrich 2010; Sutherland and Melville 2015; Thomson et al. 2016; Zippel et al. 2018). By using a gradient diffusion hypothesis, Craig and Banner (1994) developed an analytical solution for the diffusive-dissipative balance within the wave transport layer:

$$\frac{\varepsilon z_0}{F_0} = A\left(1 + \frac{z}{z_0}\right)^{\lambda} \tag{3}$$

where z_0 is the surface roughness length, which scales with wave height (Zippel et al. 2018) and is related to the dominant length scale of injected surface-generated turbulence. The rapid decay of wave-breaking turbulence typically limits direct wave breaking effects on OSBL turbulence to depths shallower than $\sim 10H_s$ (Terray et al. 1996; Sutherland and Melville 2015; Gerbi et al. 2009), such that wave-breaking is likely a dominant pathway for exchange processes close to the air-sea interface, but may not play a significant role in driving entrainment near the base of the mixed layer (up to $O(100\text{ m})$ deep).

The interaction between Stokes drift and wind-forced surface shear provides another mechanism through which waves can act to modify OSBL turbulence through conversion of vertical vorticity into streamwise vorticity in a process predominantly attributed to the Craik-Leibovich vortex force (CL2, Craik and Leibovich 1976; Leibovich 1983). The resulting Langmuir circulations (Langmuir 1938) are characterized by large, horizontal counter-rotating vortices that are generally aligned down-wave, which often have visible signatures (e.g. windrows) associated with surface-convergent downwelling zones (Weller and Price 1988). In a fully turbulent, weakly-stratified OSBL, transient Langmuir cells form and dissipate episodically across a range of scales in a regime known as Langmuir turbulence (L.T., McWilliams et al. 1997). Numerical studies of LT based Large Eddy Simulations (LES) have reproduced coherent wave-aligned vortices that are generally consistent with field observations (Skyllingstad and Denbo 1995; McWilliams et al. 1997; Min and Noh 2004; Sullivan et al. 2007; Grant and Belcher 2009); however, as noted by D'Asaro et al. (2014) comprehensive measurements of OSBL dynamics needed to characterize the dependency of mixed layer turbulence on surface waves are rare (Plueddemann et al. 1996; Smith 1998; Sutherland and Melville 2013). In contrast to open open studies (D'Asaro et al.

Accepted for publication in *Journal of Physical Oceanography*. DOI 10.1175/JPO-D-23-0136.1.

2014; Li et al. 2009; Kukulka et al. 2009), detailed comparisons of data and theory made using shallow-water observations (Gargett et al. 2004; Gargett and Wells 2007; Tejada-Martinez and Grosch 2007; Gerbi et al. 2008; Kukulka et al. 2012; Scully et al. 2015; Zippel et al. 2020) have reported full-depth Langmuir cells (Gargett and Wells 2007) and significant distortion by tidal shear or bottom boundary layer turbulence (Kukulka et al. 2011; Gargett and Wells 2007; Scully et al. 2015) have been reported. Previous observations have shown that LT acts to enhance vertical turbulent velocity variance, $\langle w^2 \rangle$, by up to a factor of two relative to comparable measurements made near a rigid boundary (Tseng and D'Asaro 2004; D'Asaro 2001) and that vertical motions associated with LT tend to be strongly negatively skewed (Scully et al. 2015).

The relative roles of wave breaking and Stokes production in energizing the near-surface and structuring TKE within the mixed layer remains an open question. LES simulations that include representations of wave breaking and the vortex force have shown that the energetic whitecapping may disrupt LT development (Sullivan et al. 2007; Kukulka and Brunner 2015) and that the redistribution of wave breaking turbulence by large-scale LT cells can lead to locally enhanced short-term dispersion rates under convergence zones (Kukulka and Veron 2019). In the absence of wave breaking, TKE dissipation is thought to be balanced by Stokes production for $|z/H_s| < 0.3$, below which the turbulent TKE flux driven primarily by LT downwelling jets plays a dominant role in transporting near-surface turbulence deeper into the mixed layer (Grant and Belcher 2009). In contrast, Scully et al. (2016) showed that for observations collected in Chesapeake Bay in which LT was detected (Scully et al. 2015), TKE dissipation was balanced by a vertical divergence in pressure work consistent with wave breaking turbulence dominating the vertical transport of TKE at $|z/H_s| < 7$, where the Eulerian shear was an order of magnitude less than expected by wall layer scaling (Fisher et al. 2018b) and LT was significantly distorted by tidal shear (Scully et al. 2016).

In this study, we present observations of LT in a stratified shelf sea including a characterization of the strength and geometry of near-surface circulation as well as the spatial heterogeneity of TKE dissipation. This work contributes to a small number of studies that have documented differences in turbulent quantities measured inside and outside of LT convergence zones and the role(s) of bubbles in structuring that spatial signature (Thorpe et al. 2003b; Gemmrich 2012; Zippel et al. 2020). The observations and analysis framework are described in §2; we show in §3 that the large-coherent vortices consistent with LT result in a distribution of elevated TKE dissipation rates in the

Accepted for publication in *Journal of Physical Oceanography*. DOI 10.1175/JPO-D-23-0136.1.

OSBL that generally falls between law-of-the-wall and wave transport layer scaling. Finally, the specific nature of LT-driven turbulent transport of surface-generated TKE is examined in context of wave breaking and Stokes production in §4.

2. Methods

a. Data Collection

Data were collected using a Hydroid-Kongsberg REMUS 600 autonomous underwater vehicle (AUV). The four-meter-long, propeller-driven AUV conducted a 20 hour mission on 11-12 May 2022 approximately 1.5NM south of Santa Barbara Point, CA (34° 22' 38" N, 119° 42' 35" W) in a $\sim$ 52 m deep region of slowly varying bathymetry. The vehicle was deployed in the vicinity of Santa Barbara harbor and initially tasked with an along-shore ingress to the sampling location under front-seat (REMUS) control. Once on station, vehicle control was transferred to the backseat ROMULUS autonomy computer running MOOS-IvP software. ROMULUS was used to execute 15 transits of the stacked bowtie circuit shown in Figure 1c, which consisted of 750 m horizontal legs oriented 10^o apart at three vertical levels ($z = -2$ m , -6 m , -10 m) followed by a profiling leg in which the vehicle collected a sawtooth profile between $-45 < z < -2$ m to resolve mixed layer density structure. At the end of each circuit, a behavior timer was used to acquire a GPS fix prior to the next circuit. Traveling at a constant speed of 1.5 m/s, the vehicle completed each circuit in approximately 1 hour.

A moored Sofar Ocean Spotter wave buoy was deployed 150 m east of the northern terminus of the AUV circuit and recorded 2.5Hz GPS-based displacement measurements, from which hourly directional wave spectra were calculated using similar methods to Herbers et al. (2012). Local surface meteorological conditions were recorded by an Airmar 200WX WeatherStation mounted approximately 1.25m above the water line on a GB4A gateway transponder buoy used for acoustic communication with the vehicle during sampling. The Airmar recorded 10-minute averages of wind speed, wind direction, barometric pressure, and air temperature continuously during the experiment.

To maximize resolution of cross-wave flow structure, bowtie legs were oriented perpendicular to the predominant mean wave direction of 250^o N (Figure 1b). Swell directions in the northern reaches of the Santa Barbara Channel are largely limited to a narrow angular range out of the

Accepted for publication in *Journal of Physical Oceanography*. DOI 10.1175/JPO-D-23-0136.1.

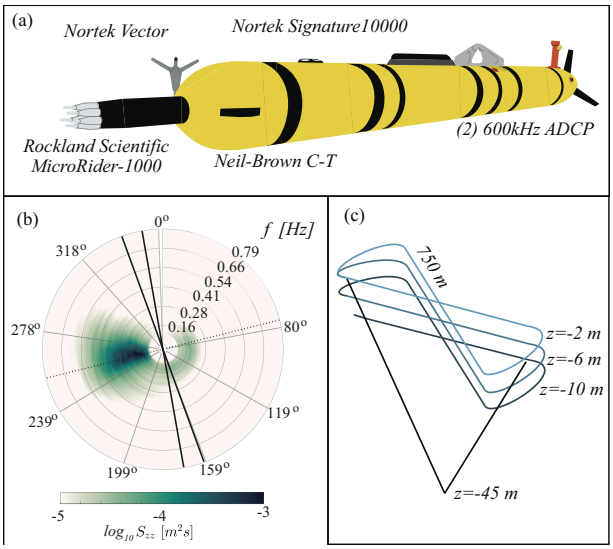

FIG. 1. (a) Schematic of REMUS 600 instrumentation. (b) Event-averaged directional wave spectra shown with orientation of mission bowtie legs (solid lines) and mean wave direction (dotted line). (c) Diagram of AUV circuit showing stacked bowtie configuration of 750 m legs.

west due to blocking and refraction induced by the presence of Point Conception and the Channel Islands. The irregular coastline, combined with high angles of incidence along the east-west coastline, results in rapid variations in wave energy arrival (Rogers et al. 2007; Crosby et al. 2019; Romero et al. 2020). Wave-current interactions associated with strong currents and complex mixed seas in the area can also lead to spatially heterogenous wave breaking (Romero et al. 2020). Additionally, the complex topography of the Santa Ynez mountains acts to shelter the region from prevailing northwest winds and increase the spatial heterogeneity of local forcing. These combined effects often result in complex mixed seas where both wind seas and swell are predominantly out of the W-WSW (O'Reilly et al. 1999).

The standard payload of the vehicle includes upward- and downward-looking 600-kHz RDI ADCPs that sampled at 1Hz with a vertical bin size of 0.5 m. The downward-looking ADCP is used as both a current profiler and Doppler Velocity Log (DVL) to measure the vehicle's altitude and horizontal velocity over the bottom. At operating depths used in this study, the DVL maintained constant bottom-lock resulting in high-fidelity estimates of speed-over-ground and geographic position. A nose-mounted Neil-Brown C-T sensor and tail-mounted Paroscientific pressure sensor recorded conductivity, temperature, and pressure, respectively, at 5Hz. The AUV is equipped with

Accepted for publication in *Journal of Physical Oceanography*. DOI 10.1175/JPO-D-23-0136.1.

a 9 degree-of-freedom Kearfott T24 inertial navigation system (INS) that samples vehicle attitude and motion at 100Hz and records 1Hz extended Kalman-filtered ouput.

In addition to house instrumentation, the AUV was equipped with a Rockland Scientific Microrider-1000 microstructure package and Nortek Signature 1000 AD2CP (Figure 1a). The microstructure package includes two orthogonal shear probes that measured vertical and transverse velocity fluctuations, a FP07 fast thermistor, and SBE7-6000 micro-conductivity sensor that sampled at 512Hz. Two orthogonal accelerometers provided synchronous measurements of transverse and vertical translational motion, also at 512 Hz. The upward-looking 5-beam Signature 1000 was mounted in the wet payload of the vehicle and configured to sample along-beam velocity profiles at 4Hz continuously at 0.5m vertical resolution. In addition to broadband current profiles, the instrument was configured to sample in echosounder mode to collect high resolution (5mm) profiles of acoustic backscatter intensity at 4Hz using the vertical 5th beam. An integrated AHRS recorded synchronous measurements of instrument motion and attitude.

b. Analysis

To distinguish circulations associated with Langmuir cells from nonturbulent fluctuations induced by surface waves, elevated volume backscattering strength, S_v, associated with entrained bubble clouds was used to map velocity measurements to cell structure assuming that observed bubble clouds were primarily structured by the strength of surface-convergent downwelling at depths greater than one significant wave height. A modified implementation of the sonar equation was used to estimate backscattering strength relative to ambient surface mixed layer conditions, $\tilde{S_v}$, which assumed a constant gain factor of the configured transducer. A sample record of backscattering strength is shown in Figure 2 for a 10-m deep leg of the bowtie circuit in which Langmuir cells were detected. Similar to recent results shown by Derakhti et al (2023), the acoustic near-field of the AD2CP is approximately ~ 1 m as indicated by increased attenuation in the vicinity of the up-looking transducer head in Figure 2. As shown in Figure 2b, observed bubble plumes with depths denoted $\mathcal{D}_{lc}$ resulted in backscattering intensities that were on average between 5-20 dB above ambient conditions, calculated as the median backscattering strength outside bubble plumes, that decayed with depth within the plume. This is similar to bubble clouds measurements reported

Accepted for publication in *Journal of Physical Oceanography*. DOI 10.1175/JPO-D-23-0136.1.

by Farmer and Li (1995), and corresponds to a 3-100 fold increase in void fraction assuming a constant bubble size distribution (Vagle and Farmer 1992).

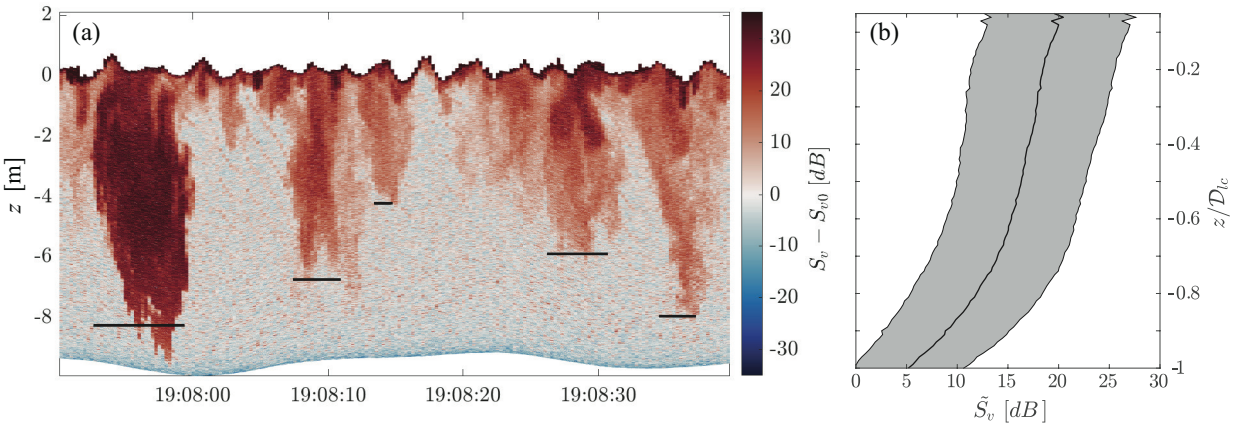

FIG. 2. (a) Sample bubble plume detection in Signature1000 echogram collected during 10m circuit leg. Horizontal black lines indicate the average depth of plumes, $\mathcal{D}_{lc}$. (b) Average profile (thick line) of residual volume backscattering strength, $\tilde{S_v}$, as a function of normalized depth within bubble plumes. Shaded area represents 1 standard deviation from the mean.

Following removal of low-frequency ($< 1/20$ Hz) platform motion, earth-relative AD2CP velocity profiles were rotated into a wave-relative coordinate system using average wave directions measured by the Spotter during each bowtie circuit. The near-neutral AUV closely follows isobars while sampling in a constant depth mode, such that vertical platform excursions within the wave frequency band are dominated by orbital motions (Fisher & Nidzieko 2023 unpublished manuscript), reducing aliasing of velocity signals by wave orbitals through sampling in a nearly wave-following vertical reference frame. Using estimates of acoustic backscatter, the downwelling centers were identified in 10-m deep horizontal transects and used to map velocity measurements to locations within individual Langmuir cells. As noted by Plueddemann et al. (1996), the direct use of backscattering intensity may introduce additional uncertainty in the estimation of circulation because stronger circulation likely entrains higher densities of bubbles in convergent downwelling zones than weaker cells. In a similar approach to that used in Zippel et al. (2020), a binary classification of backscatter profiles was made using a threshold of $\tilde{S_v} = 6.5$ dB and downwelling centers were estimated as the mean cross-wave location of individual bubble clouds (e.g. Figure 2a). Conditional-averaging was then performed to calculate an ensemble velocity field based on

Accepted for publication in *Journal of Physical Oceanography*. DOI 10.1175/JPO-D-23-0136.1.

a 2D spatial grid defined using a uniform 0.5m vertical spacing and a 10-point discretization of spanwise distance normalized by estimated cell width.

The methods above provide a framework for characterizing observed turbulent circulation in shallow, horizontal AUV transects. To assess the relative roles of wind and waves as sources of turbulent energy driving those motions, we use the turbulent Langmuir number (McWilliams et al. 1997):

$$La_t^2 = \frac{u_*}{U_{S0}} \tag{4}$$

where u_* is the water-side friction velocity and U_{S0} is the surface Stokes drift velocity. The surface value of Stokes drift in the average direction of wave propagation was calculated from measured directional wave spectra following Kenyon (1969). Due to the attenuation of wave motion due to buoy size, a f^{-4} tail was fit to observed wave spectra for $f > 0.8$ Hz. The turbulent Langmuir number represents the ratio of wind-driven shear production to the production of TKE by Stokes shear via the vortex force (e.g. Leibovich 1983) in a shallow layer where Stokes shear is significant. Alternative definitions of La_t have been suggested due to the sensitivity of U_{S0} to high-frequency surface gravity waves (e.g. Kukulka and Harcourt 2017). However, due to the tight coupling between wind stress and short waves within the equilibrium subrange, previous work has shown that La_t does not vary widely over realistic ocean conditions and generally falls between 0.2-0.5 for equilibrium conditions in the open ocean (McWilliams et al. 1997; Belcher et al. 2012). Shallow water observations have reported slightly larger values of La_t (Gargett and Wells 2007; Scully et al. 2015).

When there is sufficient heat loss at the ocean surface, the surface buoyancy flux can provide a dominant source of energy for turbulent exchange through the generation of Rayleigh-Bernard convective instabilities (Shay and Gregg 1986). To quantify the relative importance of buoyancy forcing to wave forcing, Li et al. (2005) define the Hoenikker number, which may be expressed as:

$$Ho = \frac{2B_0}{U_{S0}\beta u_*^2} \tag{5}$$

where $B_0 = \alpha g Q / C_p \rho_w$ is the surface buoyancy flux out of the ocean, $1/2\beta$ is the Stokes e-folding depth, α is the thermal expansion coefficient, Q is the net surface heat flux, and C_p is the specific heat capacity of water. Under stabilizing conditions, $Ho < -1$, it has been suggested that near

Accepted for publication in *Journal of Physical Oceanography*. DOI 10.1175/JPO-D-23-0136.1.

surface stratification prevents the generation of Langmuir turbulence. Similarly, the transition to a convection-dominant regime is thought to occur at $Ho > 1$.

Bulk air-sea fluxes were estimated from surface measurements, in combination with subsurface temperature observed by the AUV in the upper 2m of the water column, using the COARE 3.5 algorithm (Fairall et al. 2003; Edson et al. 2013). Net shortwave and longwave radiation was not measured directly, instead estimates were obtained from the NCEP North American Regional Reanalysis model for the grid cell closest to the study domain. In addition to bulk wind stress, the momentum flux required to maintain a balance between wind energy input and dissipation within the equilibrium subrange of the wave field was calculated using the Phillips (1985) analytical expression for the wave energy spectrum within the equilibrium subrange:

$$F(f) = \frac{4\beta I(p) g u_{eq}}{8\pi^3 f^4} \tag{6}$$

where $F(f)$ is the wave displacement spectra as a function of cyclic frequency (f), β is an empirical constant, $I(p)$ is a directional spreading function, and u_{eq} is the air-side friction velocity required to maintain the wave field. Assuming stationary and homogeneous wind forcing, spectral levels within the equilibrium subrange are entirely determined by the balance between generation, dissipation, and redistribution by nonlinear wave-wave interactions such that the tail of the wave spectrum responds rapidly to changing wind conditions and is thought to support the majority of aerodynamic drag (Janssen 1989). Contained within this assumption, this approach presumes that wave direction within the equilibrium subrange closely follows wind direction. The equilibrium stress therefore provides an alternative estimate of the momentum flux transmitted to the water column through the wave field and has been shown to capture momentum sinks associated with the growth of young sea states (Fisher et al. 2017).

Following Banner (1990), the equilibrium subrange is defined here as $f > 2f_p$, where f_p is the peak wave frequency. Uncertainty in the empirical growth rate, β (Plant 1982), is a principal source of uncertainty in the application of equation 6 as previously reported values vary by approximately a factor of 2 (Phillips 1985; Juszko et al. 1995; Voermans et al. 2020).By comparing observed wind speed and wave spectra, Voermans et al. (2020) found that for 10-meter wind speeds greater than 6 m/s, observations were reasonably approximated using a constant value of $\beta = 0.009$, which is slightly less than the originally proposed value of 0.012 (Phillips 1985; Thomson et al. 2013).

Accepted for publication in *Journal of Physical Oceanography*. DOI 10.1175/JPO-D-23-0136.1.

To estimate u_{eq}, equation 6 was fit to measured wave spectra within the equilibrium subrange assuming $\beta = 0.011$ and $I(p) = 2.44$. The value of the spreading parameter was determined from spectral moments following (Thomson et al. 2013) and averaged for periods when wind speeds exceeded 5 m/s.

LT effects on turbulent exchange within the surface mixed layer were evaluated through analysis of dissipation rates estimated from measured microstructure shear spectra. Assuming isotropy in the inertial subrange, the rate of turbulent kinetic energy dissipation is related to shear as follows (Oakey 1982):

$$\varepsilon = \frac{15}{2}\nu\overline{\left(\frac{\partial v}{\partial x}\right)^2} = \frac{15}{2}\nu\overline{\left(\frac{\partial w}{\partial x}\right)^2} = \frac{15}{2}\nu\int_0^\infty \Psi(k)\,dk \tag{7}$$

where ε is the turbulent kinetic energy dissipation rate, ν is the kinematic viscosity, $\Psi(k)$ is the wavenumber shear spectra, and v and w are transverse and vertical turbulent velocity fluctuations, respectively, measured along an x-axis aligned with the vehicle's centerline. The following methods are similar to previosuly reported results using this platform (Fisher et al. 2018a). Shear spectra were estimated from measured shear signals over 3-second data increments via ensemble averaging of five 512-point FFT using a 50% overlapped cosine window. The corresponding FFT spatial length of 1.5 m adequately resolves the inertial subrange even at low dissipation rates and ensures high degrees of freedom for the observed range of dissipation rates; the resulting ensemble-averaged spectra have a spatial resolution of 4.5 m. Spatially-averaging due to the finite size of the airfoil shear probes was adjusted following Macoun and Lueck (2004) using a half-power wavenumber response of 48 cpm. Prior to integration, the adjusted shear spectra were despiked and detrended using a 0.5 Hz high-pass Butterworth filter. The integrated Microrider accelerometers were used to correct for vehicle motion following the spectral method outlined in Goodman et al. (2006). Using RSI ODAS v4.2 MATLAB code, dissipation rates were then estimated from Nasmyth empirical spectra (Oakey 1982) by first integrating observed shear spectra for wavenumbers less than 10 cpm. Based on this initial estimate, dissipation rates were calculated using either an integration (variance) method or fitting the inertial subrange of the observed spectra to Nasmyth spectra. The variance method was used for dissipation rates less than 1 x 10^{-5} m^2 s^{-3}, which applied to nearly all of the data. The upper limit of integration was determined by the initial dissipation estimate and was restricted to wavenumbers between 10 cpm and 150 cpm (e.g. Lueck 2016).

Accepted for publication in *Journal of Physical Oceanography*. DOI 10.1175/JPO-D-23-0136.1.

At approximately 04:00 UTC on May 12, the responsiveness of both the orthogonal shear probes and FP07 suddenly degraded, possibly due to the probes hitting an object in the water column. The resulting microstructure shear and temperature signals collected during the 7-15th AUV circuits were nonphysical and omitted from the analysis. To assess the quality of the remaining data, goodness of fit between observed shear spectra and Nasmyth curves was evaluated using the figure-of-merit parameter, $FoM = MAD \times DOF^{1/2}$, which combines degrees-of-freedom (DOF) and the mean absolute deviation (MAD) into one misfit estimate that generally captures conditions when observations agree well ($FoM < 1$) with the Nasmyth shape and when they do not ($FoM >> 1$). Observations departed significantly from Nasmyth curves when $FoM > 1.1$, which is slightly more conservative than criterion previously reported (Fer et al. 2022). Additionally, any spectra that passed the FoM criterion for which the ratio $\Psi(k)$ to the Nasmyth curve differed by at least one order of magnitude within the inertial subrange was omitted. Approximately 5% of the data failed to meet these criterion and were omitted from further analysis.

3. Results

a. Wind, Wave, and Buoyancy Conditions

The May 11 event was driven by sustained 10 m s^{-1} westerly winds that lasted 10 hours and rotated from 230-330 ^{o}N following the passage of an atmospheric warm front (Figure 3). The event built mixed seas with significant wave heights that reached 1.5 m with average wave periods of 4 seconds. Following Wang and Hwang (2001), wave spectra were partitioned into wind sea and swell components by finding a separation frequency defined using wave steepness:

$$\alpha(f_*) = \frac{8\pi \int_{f_*}^{f_{max}} f^2 F(f)\, df}{g \left[\int_{f_*}^{f_{max}} F(f)\, df \right]^{1/2}} \tag{8}$$

where α is a frequency dependent steepness function that describes the average steepness or waves at frequencies above f_* [Hz]. The characteristics of $\alpha(f_*)$ are strongly related to short wind waves as reflected by the dependency on f^2 in equation 8 and its cumulative nature reduces sensitivity to spectral irregularities. A separation of frequency, f_s, that separates wind sea from dominant swell is then defined as the peak frequency of the steepness function.

Accepted for publication in *Journal of Physical Oceanography*. DOI 10.1175/JPO-D-23-0136.1.

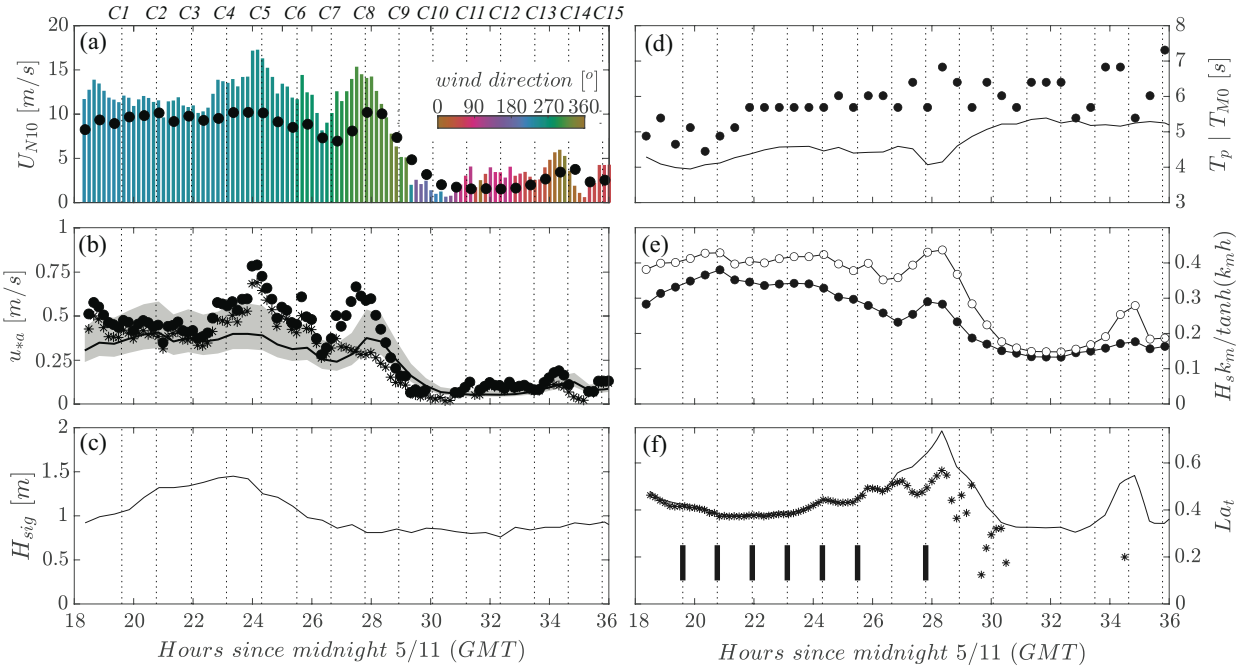

FIG. 3. (a) Ten-meter neutral wind speed estimated using COARE 3.5 colored by wind direction. U_{N10} values estimated using u_{eq} and COARE 3.5 wave-slope dependent roughness also shown as markers. (b) Bulk air-side shear velocity (circles) shown with equilibrium shear velocity estimated from observed wave spectra (solid line). Gray shaded area corresponds to u_{eq} values resulting from uncertainty in β as reported by Juszko et al. (1995). Asterisks indicate bulk flux estimate which has been corrected for wave-induced pressure fluctuations as described in the text. (c) Significant wave height. (d) Peak (markers) and energy-weighted (line) wave period. (e) Bulk wave steepness of wind sea (white markers) and mixed wave field (black markers). (f) Turbulent Langmuir number estimated via eq. 4 (solid line) and using relative angle between wind and waves (markers). Solid black bars indicate periods when Langmuir cells were detected in Signature1000 echograms. Vertical dotted lines in all panels indicate mean time of AUV circuits labeled sequentially C1-C15.

Throughout the wind event, in which measured wave spectra exhibited a clear f^{-4} spectral slope at high frequencies (Figure 4), the equilibrium subrange estimate of the air-side friction velocity (u_{*a}) was less than the COARE 3.5 estimate and exhibited less temporally variability (Figure 3c). The event-averaged wave age, defined as c_p/u_{*a} where c_p is the phase speed associated with the peak frequency of the wind sea, was 18.2 with the youngest recorded wave age being 11. A common threshold that is used to define the point at which a wave field can be considered fully

Accepted for publication in *Journal of Physical Oceanography*. DOI 10.1175/JPO-D-23-0136.1.

developed is $c_p/u_{*a} \approx 32$ (Donelan 1990; Edson et al. 2013), such that young wave ages measured in this event suggest that the wind sea was in an active state of growth towards equilibrium.

Comparison of COARE 3.5 estimates of U_{N10} with other available nearby observations (NDBC stations NTBC1 and 46053) indicates that the high frequency variation present between 22-27 hours after midnight 5/11 was inconsistent with other regional time series of the wind event and exceeded offshore wind speeds (NDBC 46053). In contrast, estimates of U_{N10} based on u_{eq} using COARE 3.5 wave-dependent formulations of roughness defined by Edson et al. (2013) and calculated following Voermans et al. (2020) did not exceed 15 m/s or exhibit similar large peaks. Given the measurement height of the Airmar (1.25 m), which was comparable to the significant wave height during the experiment, it is possible that bulk estimates of U_{N10} were biased high by preferentially sampling wave-coherent airflow in the atmospheric wave boundary layer (WBL, Janssen 1989) and periodic sheltering of the anemometer by large wave crests. Previous studies have demonstrated that mean wind profiles within the WBL can decrease more rapidly than expected for a log profile leading to an overestimation of 10-meter conditions when adjusted from the measurement height (Babanin et al. 2018; Husain et al. 2022).

Corresponding air-side friction velocity estimates are shown in Figure 3b. Equilibrium stress values corresponding to previously reported uncertainties in the empirical growth rate ($\beta = 0.0122 \pm 3.6 \times 10^{-3}$ Juszko et al. 1995) are shown as well as u_{*a} estimates that have been corrected for wave-coherent airflow following Hristov and Ruiz-Plancarte (2014) (equation 25 therein). We note that, like mean wind speed measurements, parameterized β values do not account for changes in the ratio of wind curvature to shear (Miles 1957) or other modifications to an assumed logarithmic near-surface wind profile (Plant 1982; Janssen 1989, 1991). The Janssen (1999) formulation of the pressure work term within the atmospheric TKE budget was used to specify a reasonable wind deficit that decayed exponentially with height. Following subtraction of the estimated wind deficit from measured wind speed, COARE 3.5 was re-run on the adjusted time series to produce new estimates of u_{*a}. Uncertainty in β corresponds to an approximately 30% change in estimates of u_{eq} and correcting for wave-induced pressure effects reduced bulk u_{*a} (U_{N10}) estimates by 15% (10%). We note that during the beginning of the record both estimates largely overlap; however, wind-wave misalignment contributed to increased uncertainty in both parameters at the end of the wind event (Hours 26-29). Additionally, the unusual peaks in bulk estimates of U_{N10} could not be accounted

Accepted for publication in *Journal of Physical Oceanography*. DOI 10.1175/JPO-D-23-0136.1.

for using a constant height adjustment for wave-induced pressure effects. Without direct, spectral wind stress measurements and given the possible bias in GB4A wind measurements, u_{eq} was used as a direct proxy of u_{*a} for the remainder of analysis.

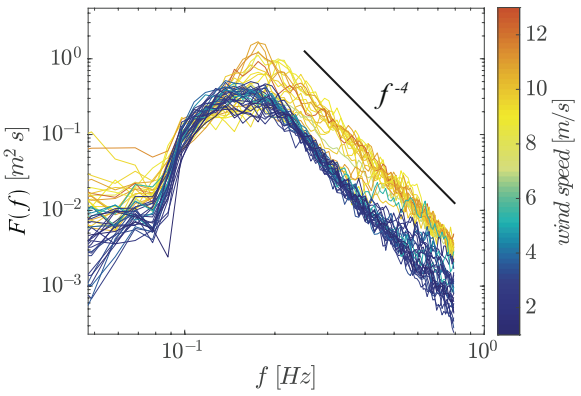

FIG. 4. Spotter surface displacement spectra colored by observed wind speed. During the wind event, a clear f^{-4} equilibrium subrange is present.

Values of La_t calculated using u_{eq} averaged 0.4 during the wind event (Figure 3c). Because of the relative angle between average wave direction and wind direction (θ_{ww}) varied by as much as 60 degrees during the event, an estimate of La_t that accounts for wind-wave misalignment, $La_t^2 = u_* \cos(\theta_{ww})/U_{S0}$, is also shown. During periods when Langmuir cells were detected, both formulations of La_t resulted in similar ratios of wind to wave forcing. As such, equation 4 was used in scaling analysis for the remainder of the paper. Estimates of Ho based on COARE 3.5 bulk fluxes indicate that generally $|Ho| < 0.1$ during periods when $La_t < 0.5$, with values of $0 < Ho < 0.01$ associated with destabilizing surface buoyancy fluxes. As winds relaxed and the surface buoyancy flux became negative, $Ho < -0.1$ indicating that a stabilizing surface heat flux was generally not strong enough to prevent LT generation during the latter half of the event (not shown).

Direct measurements of breaking waves are difficult, often requiring visual detection of individual whitecaps at the sea surface which were not collected during this study. Rather, bulk wave steepness was used to estimate breaking rates based on spectral observations utilizing a parametric breaking model. Bulk steepness was calculated based on both the full spectrum and the wind sea following equation 9.

$$s = \frac{H_s k_m}{\tanh(k_m d)} \tag{9}$$

Accepted for publication in *Journal of Physical Oceanography*. DOI 10.1175/JPO-D-23-0136.1.

The mean wavenumber, k_m, in equation 9 is calculated using linear wave theory given water depth, d. Results shown in Figure 3f indicate that throughout the event, $s < 0.4$ consistent with limiting steepness values reported in previous studies (Drazen et al. 2008; Filipot et al. 2010; Zippel and Thomson 2017) conducted in deep to intermediate wave environments. Bulk steepness ranged between 0.2-0.35 for the full spectrum and 0.28-0.39 within the wind sea during periods of sustained wind forcing, which corresponds to an average breaking fraction of 7.5×10^{-3} and 1.5×10^{-2}, respectively, when estimated using the Chawla and Kirby (2002) single-parameter breaking model. These relatively high breaking fraction estimates indicate that energetic whitecapping was likely occurring throughout the event; serving as a dominant pathway for the transfer of momentum and energy into the water column.

Throughout the wind event, the upper 40m of the water column remained weak to moderately stratified (Figure 5a) and exhibited nearly linear stable stratification during the first 4 hours of the experiment. Surface mixed layer depth, H_m, estimated as the minimum depth for which $N^2 > 9 \times 10^{-5}\ s^{-2}$, deepened from 19m to 26m between 19:00-23:00 UTC on May 11 before rapidly shoaling to 4m when a well-mixed, deep water mass moved north onto the shelf (Figure 5b,c). The observed deepening rate of ~ 2 m hr^{-1} was consistent with the simple analytical model proposed by Trowbridge (1992) for a wind-forced, rigid-lid OSBL with linearly-varying stable stratification:

$$H_m \frac{\partial H_m}{\partial t} = C Ri_c^{1/2} \frac{u_*^2}{N} \tag{10}$$

where $C = 1.22$ is an empirical constant and $Ri_c = 1/4$ is the critical value of the gradient Richardson number. Average values of u_* and $\overline{N}_{20}$ over first four AUV circuits were used in equation 10, where $\overline{N}_{20}$ is depth-averaged value of the Brunt-Väisälä frequency (N) over the upper 20 m of the water column. In contrast to observations by Smith (1992) and Plueddemann et al. (1996), this suggests that wave-driven mixing did not play a significant role in deepening the mixed layer during this experiment. Current speeds within the surface mixed layer exceeded 35 cm/s near the surface with significant shear (Figure 6) near the base of the mixed layer that changed rapidly in response to wind and baroclinic forcing.

Accepted for publication in *Journal of Physical Oceanography*. DOI 10.1175/JPO-D-23-0136.1.

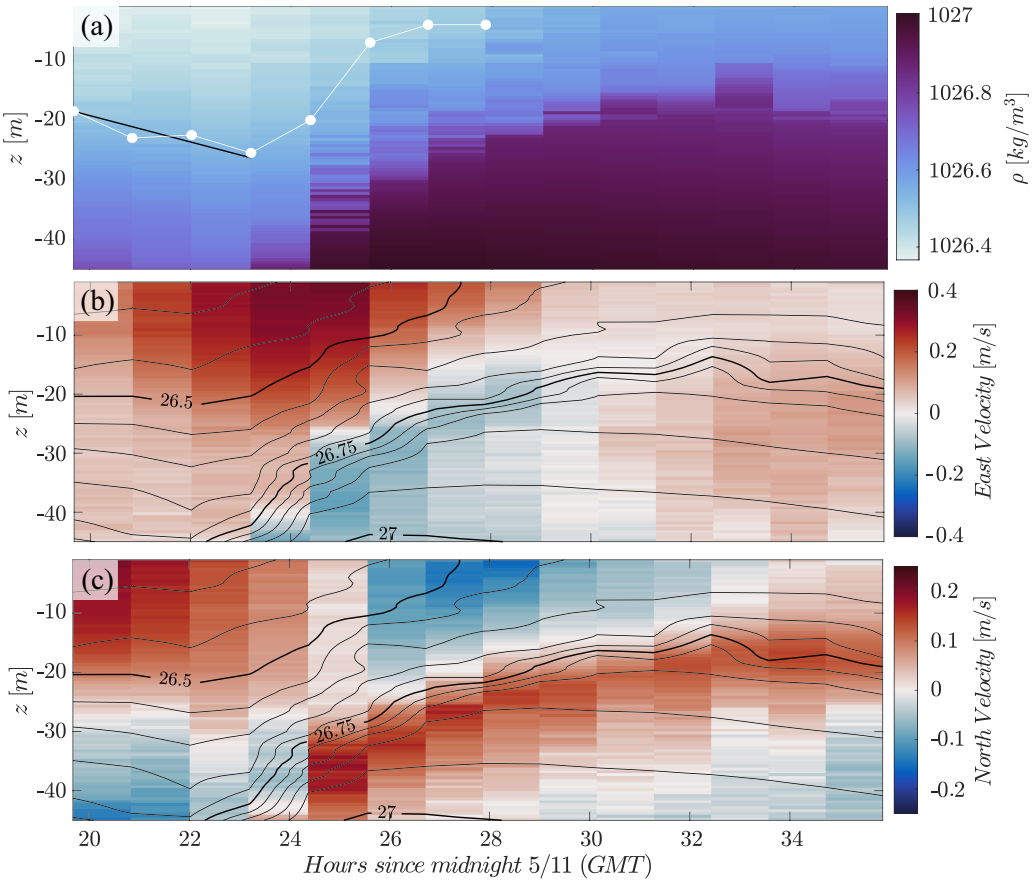

FIG. 5. (a) Density structure shown with mixed layer depth (white line) estimated using a threshold of $N^2 = 9 \times 10^{-5}$. The Trowbridge (1992) analytical KP solution for mixed layer deepening is shown as a black line. East/west (b) and north/south (c) water velocities shown with density anomaly contours.

b. Langmuir Cell Structure

Bubble clouds extending to 9 m deep were detected in AD2CP echograms during the first eight circuits of the AUV mission as depicted in Figure 3f. Cell geometry was inferred from acoustic bubble signatures, such that the depth of individual plumes was estimated as the maximum depth for which the median backscatter at a given depth within a plume exceeded background levels by $4dB$. Plume depth, $\mathcal{D}_{lc}$, was then determined from plume-averaged vertical backscatter profiles, which were spatially-averaged using a 0.5 m centered window. Horizontal cell spacing, $\mathcal{W}_{lc}$, was calculated as the across-wave distance between adjacent downwelling centers, such that individual vortex widths were estimated as $\mathcal{W}_{lc}/2$. Distributions of bubble plume depth and spacing measured

Accepted for publication in *Journal of Physical Oceanography*. DOI 10.1175/JPO-D-23-0136.1.

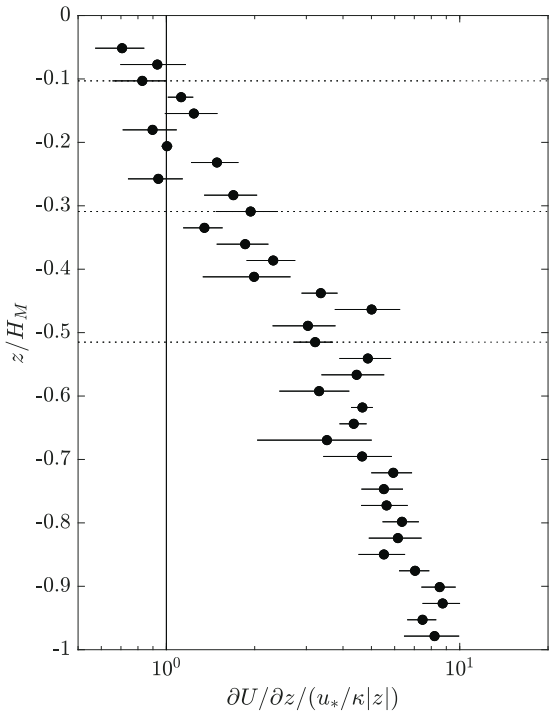

FIG. 6. Bin-averaged vertical shear normalized by wall layer scaling shown with standard error bars as a function of depth within surface mixed layer. Horizontal dashed lines indicate sampling depths of 2 m, 6 m , and 10 m.

during periods when LT was present are shown in Figure 7. The median plume depth varied little during the first six hours of the event when Ho was positive, deepening from 6 m to 6.5 m before decreasing to 5.5 m during periods when $-0.1 < Ho < 0$. Horizontal cell spacing appeared lognormally-distributed with the majority of observations falling below the average mixed layer depth a median value close to 14 m during the first six hours of the experiment. These results are comparable to previously reported backscatter associated with Langmuir turbulence (Farmer and Li 1995; Thorpe et al. 2003a); however, no accompanying measurements of cloud depths were available in those studies. As stratification increased, W_{lc} increased to $\sim$ 30 m. Sparse $\sim$ 5 m deep bubble clouds were detected during the ninth circuit, but were too few in number to estimate cell statistics. Favorable values of La_t and Ho during this period suggest that cell formation was suppressed due to rapid shoaling of isopycnals and/or a reduction in wave breaking resulting in a highly intermittent field of downwelling injections rather than a well-developed LT field. A

Accepted for publication in *Journal of Physical Oceanography*. DOI 10.1175/JPO-D-23-0136.1.

TABLE 1. Summary of surface mixed layer length scales observed during C1-C6 shown in meters.

Circuit	Langmuir cell depth ($\mathcal{D}_{lc}$)	Horizontal Langmuir cell spacing ($\mathcal{W}_{lc}$)	Mixed layer depth (H_m)	Critical mixing depth ($\tilde{h}$)
C1	6.0 ± 1.1	14.8 ± 6.1	18.5	7.0
C2	7.0 ± 1.2	14.0 ± 6.8	23.0	7.5
C3	6.4 ± 1.1	17.5 ± 9.1	22.5	7.0
C4	6.6 ± 1.2	16.8 ± 7.4	20.0	8.5
C5	6.0 ± 1.1	14.8 ± 6.1	18.5	8.0
C6	6.0 ± 1.1	22.7 ± 13.5	7.0	5.5

summary of length scales associated with observed LT cells and mixed layer stratification is shown in Table 1.

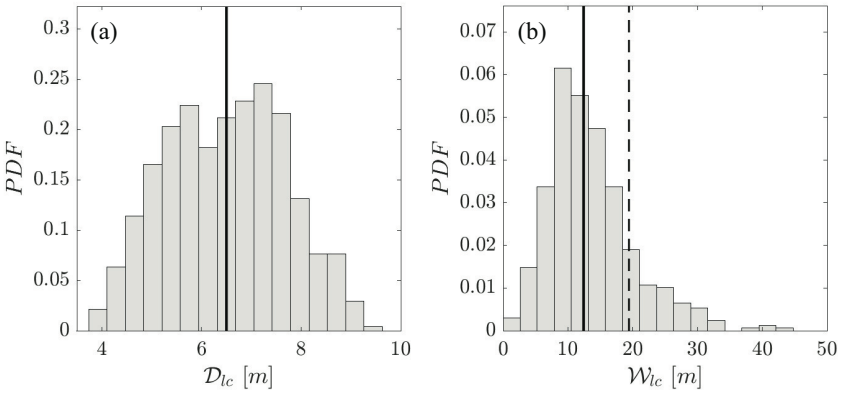

FIG. 7. Langmuir cell statistics during the May 11 wind event: (a) cell depth and (b) cross-wave cell spacing. Thick vertical lines in both panels indicate median value of the distribution. The dashed line in panel (b) indicates the average mixed layer depth.

Conditionally-averaged AD2CP vertical velocities indicate that observed bubble clouds were coincident with intensified downwelling jets flanked by broader, weaker upwelling zones consistent with surface convergent counter-rotating cells typical of Langmuir turbulence (Figure 8). In an ensemble sense, the spanwise extent of downwelling regions was approximately 67% that of upwelling regions with corresponding depth-averaged velocity magnitudes that were generally more than twice as strong. By assuming a balance between Stokes shear production and TKE dissipation, several studies have suggested that the appropriate velocity scaling for Langmuir turbulence is (Smith 1996; Min and Noh 2004; Harcourt and D'Asaro 2008; Grant and Belcher

Accepted for publication in *Journal of Physical Oceanography*. DOI 10.1175/JPO-D-23-0136.1.

2009; Belcher et al. 2012; Sutherland et al. 2014):

$$w_{*L} = \frac{1}{La_t^{2/3}} u_* = \left(u_*^2 U_{S0}\right)^{1/3} \tag{11}$$

The vortex force acts to increase vertical and transverse turbulent kinetic energy variance above values expected for wall-bounded shear flows, which has been documented by a number of prior observational (D'Asaro 2001; Tseng and D'Asaro 2004; Scully et al. 2015) and numerical LES studies (Min and Noh 2004; Li et al. 2005; Sullivan et al. 2007; Grant and Belcher 2009). Depth-averaged vertical velocities shown in Figure 8a agree well with w_{*L} with normalized downwelling intensities close to 1 near the ocean surface, supporting the use of equation 11 as the appropriate scaling for Langmuir turbulence. Vertical turbulent kinetic energy (VKE) estimated as the spanwise-averaged vertical velocity squared, $< w^2 > /u_*^2$, decayed rapidly with depth in a manner consistent with previous studies of Langmuir cells in homogeneous water (Figure 8c). Observations agree well with recent LES results by Kukulka and Harcourt (2017) for monochromatic wave conditions defined using the peak wavenumber of the wind sea ($k = 0.63$ m $^{-1}$) in the absence of stratification. In contrast to the monochromatic conditions simulated in that study, mixed seas present during this experiment had Stokes drift decay scales that were dominated by the wind sea near surface and increased with depth due to the presence of swell. A clear subsurface maxima was present below $z = -1.5m$, suggesting that the peak of the VKE profile was not resolved and may have been closer to the surface as demonstrated by numerous LES studies (e.g. Figure 8c).

To determine the impact of stable stratification on the distribution of VKE, a critical mixing depth is calculated using a Langmuir Froude number (equation 12) similar to that defined by Li and Garrett (1997).

$$Fr_{lc} = \frac{w_{*L}}{N\tilde{h}} \tag{12}$$

When F_{lc} is high, downwelling jets associated with LT may penetrate stable stratification and entrain water leading to a deepening of the surface mixed layer (e.g Kukulka et al. 2010) before eventually reaching a stable limit ($z = \tilde{h}$) when wave-driven mixed layer deepening is arrested. A critical value of $Fr_{lc} = 0.5$, which is slightly less than $Fr_{lc} = 0.6$ originally suggested by Li and Garrett (1997), yields mixing depths that averaged 7m and agreed well with observed distributions of D_{lc} shown in Figure 7a as well as ensemble cell velocity profiles shown in Figure 8. Critical

Accepted for publication in *Journal of Physical Oceanography*. DOI 10.1175/JPO-D-23-0136.1.

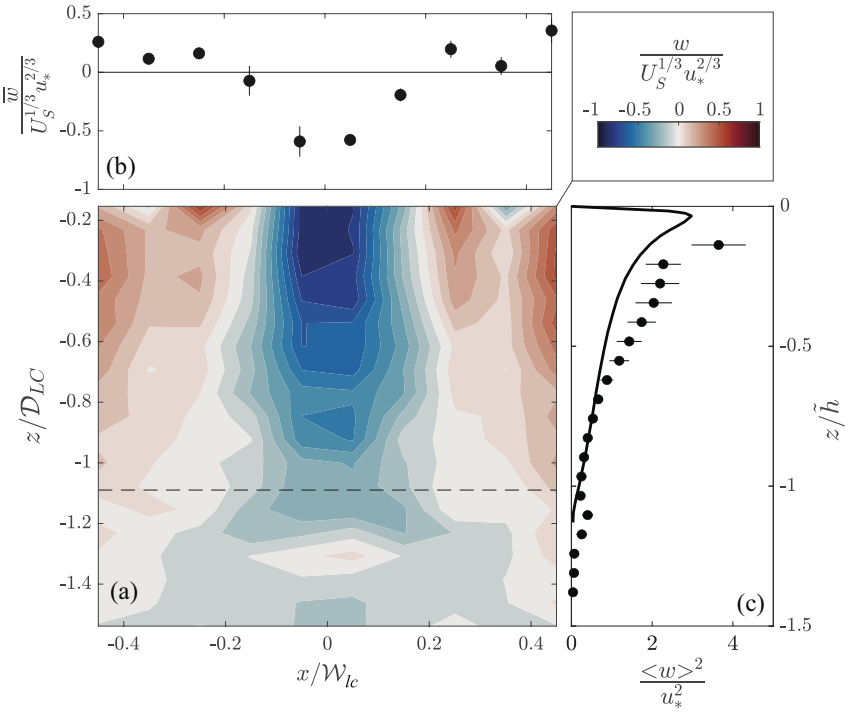

FIG. 8. Conditionally-averaged vertical velocities as a function of transverse distance from downwelling center. (a) Depth-averaged vertical velocity for $z \geq \tilde{h}$ as a function of distance normalized by cell width. (b) Vertical velocity structure as a function of normalized cross-cell distance and depth. In both panels vertical velocities have been normalized by w_{*L}. (c) Normalized VKE profile shown with Kukulka and Harcourt (2017) LES results (black line) for monochromatic wave conditions ($k = 0.63$ m^{-1}). Bars in panels (b) and (c) indicate 1 standard error.

mixing depths, $\tilde{h}$, are generally consistent with the observed decay of VKE, indicating that LT penetration depth was arrested by stable stratification at $|z/H_m| > 0.35$.

Analysis of cell aspect ratios, defined as $\mathcal{W}_{lc}/2\mathcal{D}_{lc}$, indicates that LT cells had average aspect ratios close to 1 (Figure 11) similar to previous observations made in deep-water wave conditions (Plueddemann et al. 1996; Zippel et al. 2020) prior to the arrival of the deep water mass. As isopycnals shoaled, average cell aspect ratios increased to values $1.5 < \mathcal{W}_{lc}/2\mathcal{D}_{lc} < 3$, indicating that an increase in near-surface stratification contributed to a horizontal stretching of the LT field in a similar manner to previous shallow-water observations of full-depth LT Gargett and Wells (2007).

Accepted for publication in *Journal of Physical Oceanography*. DOI 10.1175/JPO-D-23-0136.1.

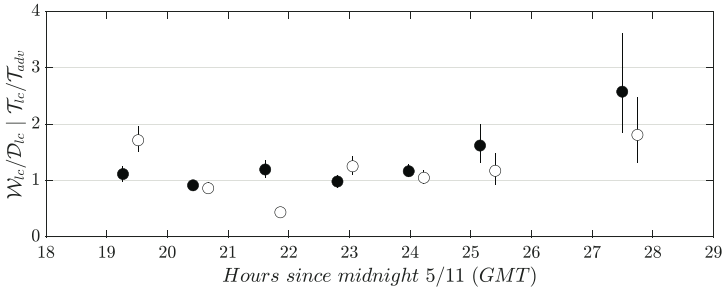

FIG. 9. Langmuir cell aspect ratio (black markers) and ratio of overturning time scale to cross-wind advective time scale (white markers) shown with 95% confidence limits.

To determine the extent to which LT cell geometry was deformed by current shear, rather than suppression of vertical motions by stable stratification within the mixed layer, an advective time scale associated with cross-wave shear is defined as $\mathcal{T}_{adv} = (\mathcal{W}_{lc}/2\mathcal{D}_{lc})(\partial V/\partial z)^{-1}$ following Kukulka et al. (2011). By comparing the advective time scale to the time scale associated with LT overturning, $\mathcal{T}_{lc} = \mathcal{D}_{lc}/w_{*L}$, the relative importance of differential advection by cross-wave sheared currents in modifying cell geometry may be assessed. Results shown in Figure 11 indicate that during times when LT was present, $0.4 < \mathcal{T}_{adv}/\mathcal{T}_{lc} < 1.8$ indicating that energetic turbulent overturning was occurring at similar time scales to differential horizontal advection within the upper water column. It's therefore likely that variable near-surface stratification and cross-shelf current structure may have acted to distort Langmuir cells, particularly during the relaxation of the wind event.

c. The vertical distribution of TKE dissipation

To characterize the vertical structure of TKE dissipation rates in the presence of LT, distributions of shear probe ε estimates were calculated as a function of normalized depth, z/H_s with H_s corresponding to the wind sea, using data from the first six AUV circuits when cell geometry statistics were relatively constant. The proportion of measurements collected at each horizontal level of the bowtie circuit are shown using stacked bar colors that denote the sampling depth. Results are shown in Figure 11 with the corresponding law-of-the-wall and wave transport layer (eq. 2) scalings as well as LES results from Sullivan et al. (2007) that included stochastic wave breaking and vortex force effects. The surface TKE flux was estimated following Craig and Banner

Accepted for publication in *Journal of Physical Oceanography*. DOI 10.1175/JPO-D-23-0136.1.

(1994) using $G_t = 90$, which is within the range of values used in previous studies of young seas at wave ages for which Terray et al. (1996) found G_t to be roughly constant. A majority of observations at $z/H_s > -7$ fell between law-of-the-wall and Terray et al. (1996) scaling with mean values generally exhibiting similar decay rate to the LES results of Sullivan et al. (2007) and previous observations made below the wave breaking layer (Thorpe et al. 2003b; Sutherland et al. 2014). At depths below $z/H_s < -7$, measured dissipation rates decayed with depth but generally exceeded all surface scaling, eventually increasing with depth for $z/H_s < -15$. Near the surface and at depths $z << \tilde{h}$, TKE dissipation was generally lognormally distributed with kurtosis and skewness values of log-transformed data close to 3 and 0, respectively (Figure 11b,c). Near the base of the wave mixing layer, ε distributions were markedly different and exhibited strong positive skew and large kurtosis values. We hypothesize that this departure from lognormality at base of wave mixing layer is indicative of energetic mixing events associated with large cells acting to penetrate stable stratification and drive intermittent injections of TKE.

4. Discussion

TKE dissipation rates exhibited a high degree of heterogeneity along horizontal AUV transects with ε often varying by over an order of magnitude over distances comparable to $\mathcal{W}_{lc}$ (Figure 11). Very few field studies have documented the horizontal variability of dissipation rates in the presence of Langmuir turbulence (Osborn et al. 1992; Thorpe et al. 2003b; Gemmrich 2012; Zippel et al. 2020), but those limited observations indicate similar heterogeneity as reported here. Similar to measurements made by Thorpe et al. (2003b) and Zippel et al. (2020), intermittent regions of elevated TKE dissipation generally coincided with elevated backscatter present in AD2CP echograms.

Conditional averaging of dissipation estimates based on AD2CP backscattering strength measured between 1-1.25m above the vehicle indicates that TKE dissipation rates were on average three times higher below downwelling centers than ambient conditions with a power-law relationship of the form $\varepsilon/\varepsilon_{amb} \sim \tilde{M_v}^b$, where $\tilde{S_v} = 10\log_{10}\tilde{M_v}$. Logarithmic regression of the data indicates b was relatively insensitive to the depth at which measurements were taken with b approximately equal to 0.2 for data collected at 2 m and 6 m depth (Figure 12). Backscattering strengths between 9 - 8.75 m depth did not span a wide enough range of $\tilde{S_v}$ to perform curve-fitting. Because the record

Accepted for publication in *Journal of Physical Oceanography*. DOI 10.1175/JPO-D-23-0136.1.

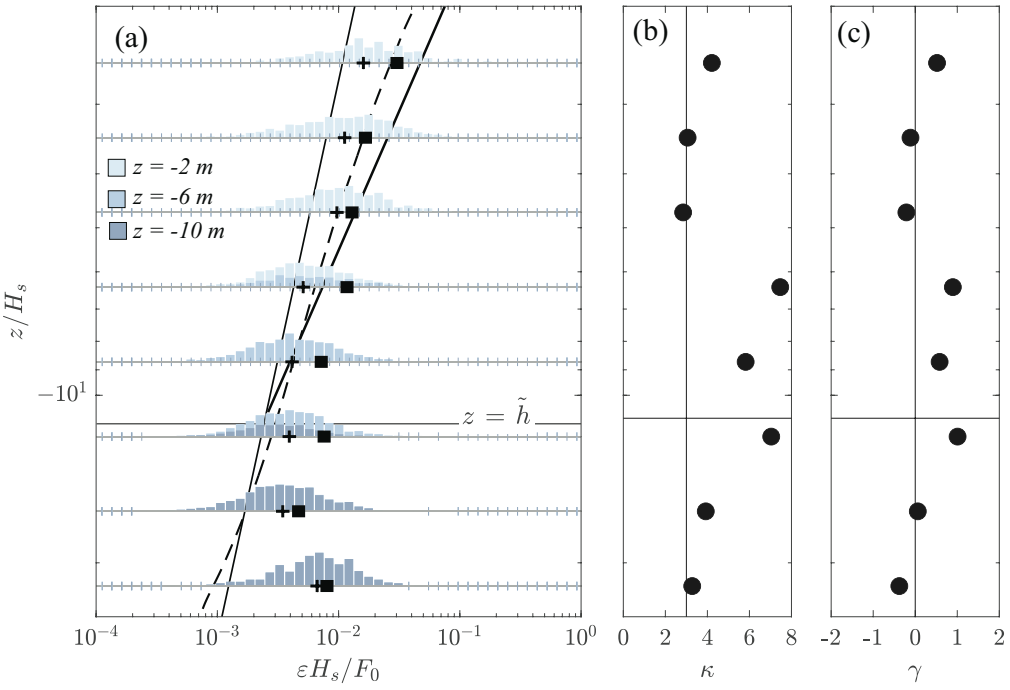

FIG. 10. (a) Vertical distribution of dissipation rate as a function of normalized depth. Median (pluses) and standard mean (squares) values are shown for each distribution with bar color indicating depth of sampling. Scalings shown include surface wall layer (thin solid line), Terray et al (1996) with $G_t = 90$ (thick solid line), and Sullivan et al (2007) LES results for combined effects of wave breaking and stokes drift (dashed line; relative to H_m). Kurtosis (b) and skewness (c) of log-transformed ε distributions as a function of normalized depth. Vertical solid lines indicate Gaussian scaling.

length used in shear probe dissipation estimates (4.5m) is comparable to the median cell width ($\mathcal{W}_{lc}/2 \sim 7$m), the averaging procedure used here to report observed enhancement of ε within LT downwelling centers may be biased low.

Consistent with prior studies that have reported elevated dissipation rates within bubble plumes beneath windrows (Thorpe et al. 2003b; Zippel et al. 2020), these results demonstrate the significant role that downwelling jets play in contributing to elevated TKE dissipation rates often observed beneath breaking waves. The monotonic increase in TKE dissipation rate with backscattering strength is consistent with the conceptual picture that stronger downwelling velocities are effective in transporting larger bubbles downward against their tendency to rise and that local shear and advection associated with energetic downwelling regions acts to elevate local dissipation rates.

Accepted for publication in *Journal of Physical Oceanography*. DOI 10.1175/JPO-D-23-0136.1.

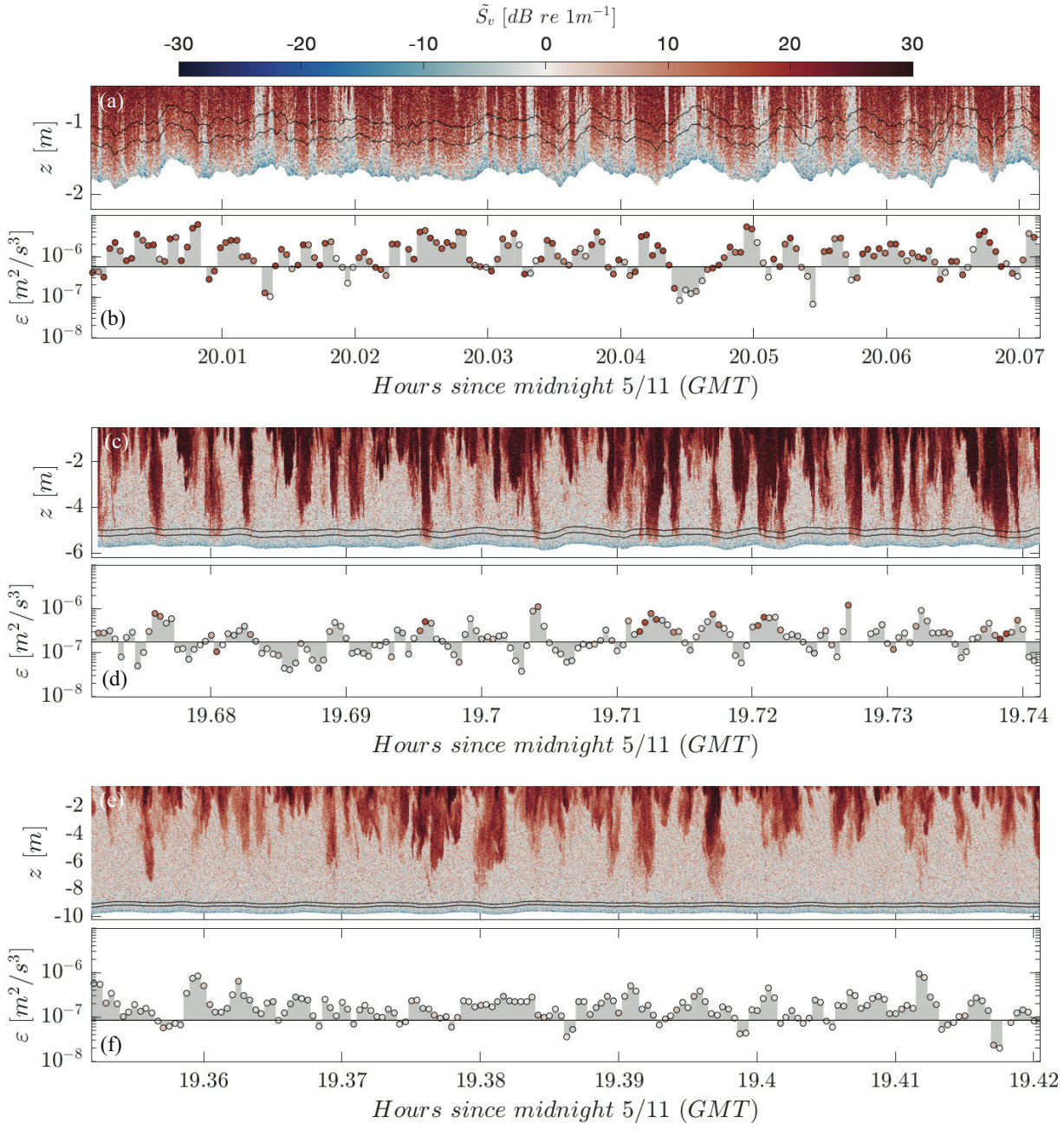

FIG. 11. Sample time series of echograms and shear probe dissipation estimates collected at (a,b) 2m, (c,d) 6m, and (e,f) 10 m depth during C1. Thin black lines in panels (a,c,e) indicate depth range of $\tilde{S_v}$ used in conditional averaging of ε. In panels (b,d,f), solid horizontal line indicates wall layer scaling and color indicates magnitude of $\tilde{S_v}$ measured 1-1.25m above transducer head.

Accepted for publication in *Journal of Physical Oceanography*. DOI 10.1175/JPO-D-23-0136.1.

However, because bubble populations may act to suppress turbulence through buoyancy stratification (Gemmrich 2012) or enhance turbulence via the generation of bubble wakes (Derakhti and Kirby 2014), further work is needed to characterize the complex roles bubbles play in mediating near surface turbulence.

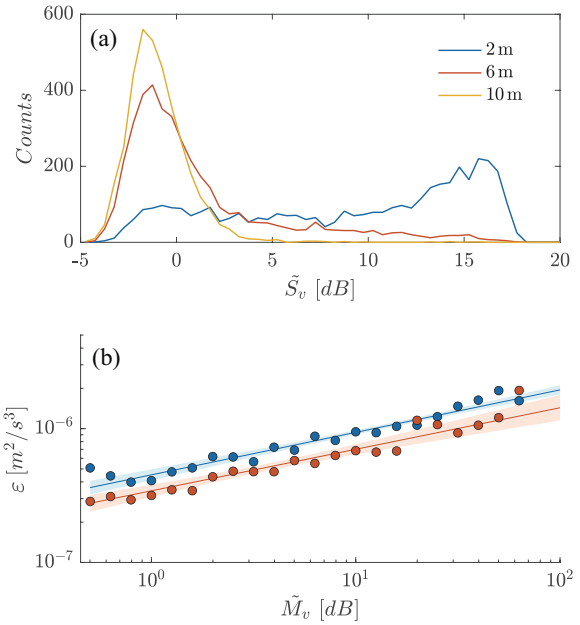

FIG. 12. (a) Distributions of backscattering strength between 1-1.25 m above AUV as a function of sampling depth. (b) Conditionally-averaged dissipation rate based on residual backscattering strength. Solid lines indicates logarithmic regression to data collected at 2 m (blue) and 6 m (red) shown with shaded 95% confidence intervals. Markers show bin-averaged dissipation data.

A number of processes may contribute to the observed enhancement of dissipation in LT downwelling zones including preferential wave breaking in the presence of surface convergences (Zippel et al. 2020) and turbulent advection of boundary-generated turbulence into the interior of the mixed layer by elevated VKE (Thorpe et al. 2003b; Kukulka and Veron 2019). A notable difference between prior studies is the observed vertical decay of TKE dissipation within the wave mixing layer with decay rates consistent with both shear-dominant, down-gradient TKE transport ($\sim z^{-1}$, Thorpe et al. 2003b; Sutherland et al. 2014) and a free-shear, diffusive-dissipative balance ($\sim z^{-2}$, Gemmrich 2012; Zippel et al. 2020) being reported. Gemmrich (2012) hypothesized that within LT convergence zones a near surface layer in which bubble-suppressed dissipation rates follow

Accepted for publication in *Journal of Physical Oceanography*. DOI 10.1175/JPO-D-23-0136.1.

equation 2, below which subducted bubbles are transported downward via TKE advection resulting in enhanced dissipation levels that follow $\sim z^{-1}$ scaling (e.g. Thorpe et al. 2003b).

Examining the vertical structure of subpopulations of ε corresponding to ambient ($\tilde{S}_v < 3$dB) conditions and within downwelling centers ($\tilde{S}_v > \tilde{S}_{v75}$, where $\tilde{S}_{v75}$ is the 75th percentile of backscattering strength measured at normalized depth z/H_s) indicates that dissipation rates inside and outside of downwelling centers decayed at similar rates proportional to z^{-1} for $|z/H_s| < 5$. The close agreement between ambient conditions and surface wall layer scaling is consistent with the observed nondimensional shear profile between 2 - 6 m depth shown in Figure 6 and suggests that LT acted to modify a background flow that was well-described by a classical wind-driven log layer. In downwelling centers, dissipation rates were nearly four times higher than ambient conditions, which is similar to estimates made by Thorpe et al. (2003b) and exhibited a nearly uniform decay rate proportional to $\sim z^{-1}$ for depths $z > \tilde{h}$ suggesting a regime in which down-gradient TKE advection was occurring.

Because direct estimates of TKE advective fluxes were not possible using this dataset, a ratio of LT overturning ($\mathcal{T}_{lc}$) to dissipation time scales is defined to determine the relative influence of vertical TKE advection in modulating observed dissipation rates. The dissipation time scale is defined as $\mathcal{T}_\varepsilon \equiv 3w_{*L}^2/2\varepsilon$ and is calculated using all dissipation rates measured between 2 - 6 m depth during the first six AUV circuits. To permit comparison of asynchronous estimates of $\mathcal{D}_{lc}$, w_{*L}, and ε, lognormal distributions were fit to observations of $\mathcal{D}_{lc}$ and used in combination with linearly interpolated values of w_{*L} to generate random estimates of $\mathcal{T}_{lc}$ of equal length to $\mathcal{T}_\varepsilon$. Results indicate that the turbulent vertical advective time scale was nearly two orders of magnitude less than the dissipation time scale, suggesting that downwelling jets were strong enough to rapidly transport surface-generated TKE downward before it dissipated (Figure 13). A more conservative estimate of $\mathcal{T}_\varepsilon$ calculated using u_* instead of w_{*L} yields a distribution of $\mathcal{T}_{lc}/\mathcal{T}_\varepsilon$ with a median value of 0.28; however, as shown in Figure 8, w_{*L} is a more appropriate scaling for large coherent eddies observed in this study. When calculated using w_{*L} and depth-averaged dissipation rates that included near surface estimates specified using equation 2, rather than individual observations collected at 2 m and 6 m depth, a mean ratio of 3.85 indicates that the advective time scale was the same order of magnitude as the dissipative time scale over the vertical extent of Langmuir cells.

Accepted for publication in *Journal of Physical Oceanography*. DOI 10.1175/JPO-D-23-0136.1.

Stokes production and wave breaking may act as dominant generation mechanisms for elevated near-surface TKE, which is then transported downward by turbulent advection. As such, it is informative to compare the relative importance of these two processes through the ratio of surface Stokes production ($U_{S0}u_*^2$, Skyllingstad and Denbo 1995) to the TKE flux generated by white-capping ($G_t u_*^3$): $U_{S0}/G_t u_*$ (Jones and Monismith 2008). Kukulka and Harcourt (2017) found that as k increases, the relative importance of TKE flux terms decreases until the Stokes decay scale becomes smaller than the surface roughness length, at which point Stokes production only acts to energize a shallow layer comparable to the depth of a wave breaking layer. Assuming that roughness length scales with wave height (Craig and Banner 1994; Zippel et al. 2018), the Stokes decay scale associated with the wind sea observed during this experiment ($1/2k \sim 0.8$ m) exceeds the surface roughness length ($z_0 = 0.3H_s \sim 0.2$ m) indicating that while conditions favored the formation of large coherent LT cells, near-surface Stokes production may have been a relatively weak source of TKE. For conditions during which LT was observed, $U_{S0}/G_t u_*$ ranged from 0.06 to 0.23 with a mean value of 0.12 indicating that F_0 was an order of magnitude larger than the surface TKE flux generated by the interaction of nonbreaking waves and currents via the CL2 vortex force.

Figure 13 shows bin-averaged dissipation profiles that have been calculated for subpopulations corresponding to ambient conditions ($\tilde{S}_v < 5$) and downwelling centers ($\tilde{S}_v > \tilde{S}_{v75}$). For depths $|z/H_s| < 5$, TKE dissipation rates outside of downwelling centers generally follow wall layer scaling while TKE dissipation rates inside downwelling zones more closely resemble scaling that arises from a diffusive-dissipative balance. This supports the conclusion that whitecapping served as the dominant source for a surface TKE flux, which was then transported down-gradient by TKE advection associated with large, coherent LT cells and demonstrates the dominant role that LT plays in redistributing TKE within the wave mixing layer. A similar result was found by Kukulka and Veron (2019), where a Lagrangian analysis of LES simulations was used to show that short-term dispersion rates associated with breaking waves can be substantially enhanced beneath surface convergence zones due to vertical transport associated with LT. The mean profile of the full dataset exhibits a decay rate similar to z^{-1} (as also evident in Figure 11a), with magnitudes that are approximately a factor of 3 larger law-of-the-wall scaling and similar to previous findings by Thorpe et al. (2003b). This suggests that wave breaking in the presence of LT may act as a significant source of TKE to depths that exceed the wave transport layer and that discrepancies

Accepted for publication in *Journal of Physical Oceanography*. DOI 10.1175/JPO-D-23-0136.1.

in the vertical decay rate of TKE dissipation in prior LT observations may be consistent with the conceptual picture proposed by Gemmrich (2012).

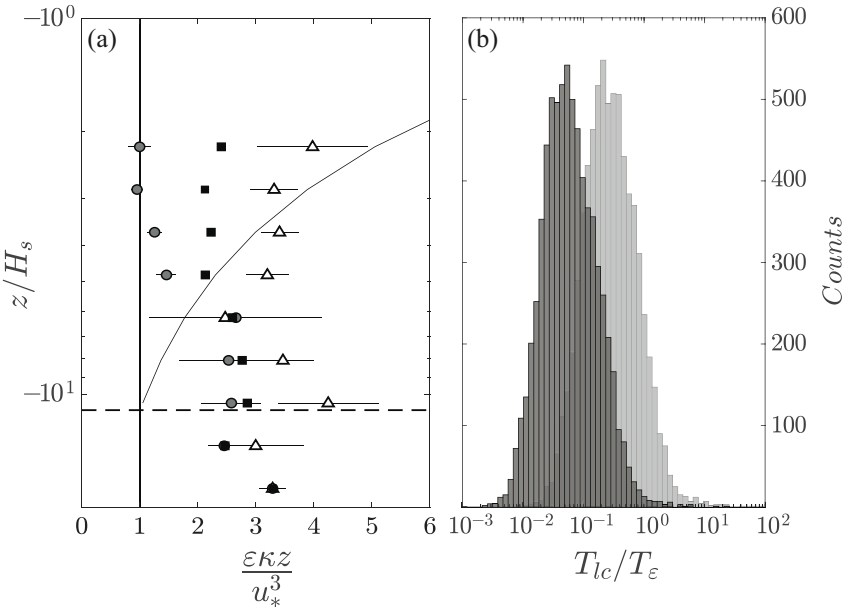

FIG. 13. (a) Detailed view of ε vertical structure in wave mixing layer where mean values for populations drawn from $\tilde{S_v} < 5$ (circles) and $\tilde{S_v} > \tilde{S}_{v75}$ (triangles) and all data (squares) are shown with 95% confidence intervals. Terray et al. (1996) scaling shown as thin solid line. Horizontal dashed line indicates $\tilde{h}$. (b) Distribution of the ratio of vertical turbulent advective time scale, $\mathcal{T}_{lc}$, to dissipation time scale, $\mathcal{T}_\varepsilon$, calculated using w_{*L} (dk. gray) and u_* (lt. gray).

5. Conclusions

Observations of large, wave-driven coherent eddies and TKE dissipation rates were collected by an AUV operating off the coast of southern California, which provide evidence that LT plays a dominant role in redistributing wave breaking turbulence within the OSBL. LT cells were limited to the upper third of the weakly-stratified mixed layer in a region where energetic downwelling zones were strong enough to erode stratification (e.g. wave-mixing layer) in a manner consistent with previous LES simulations. These downwelling jets, which were twice as strong as upwelling zones and exhibited bubble signatures proportional to void fractions nearly 2 orders of magnitude higher than the ambient fluid, had near-surface velocities that scaled as w_{*L} and decayed with depth. Conditional averaging of shear probe dissipation estimates using AD2CP backscattering

Accepted for publication in *Journal of Physical Oceanography*. DOI 10.1175/JPO-D-23-0136.1.

strength indicated that LT downwelling jets were primary drivers of a down-gradient turbulent TKE flux, which resulted in lognormally-distributed dissipation rates in the wave mixing layer with the majority of estimates falling between wall layer scaling and wave transport layer scaling. A comparison of TKE dissipation rates inside and outside of convergences demonstrates that: (1) TKE dissipation rates outside of LT convergence zones were well described by law-of-the-wall scaling consistent with the observed Eulerian shear profile; and (2) the observed enhancement of turbulent dissipation in LT downwelling zones, which was a factor of 4 higher than ambient conditions, was likely due to the vertical turbulent advection of wave breaking turbulence.

This work is motivated by the importance of surface gravity waves to the turbulent exchange of momentum, heat, mechanical energy, and gases within the OSBL. These results highlight the significant role that wave breaking turbulence and large-coherent LT cells play in structuring mixing in the upper ocean. While the relative influence of downwelling centers and vertical structure of turbulent dissipation rates are well-resolved within this dataset, uncertainty in available u_* estimates limits confidence in the overall magnitude of dissipation rates relative to surface scalings. Subtle differences in higher-order turbulent statistics across LT cells underscores the need for three-dimensional turbulence sampling to disentangle the relative roles of wave breaking and LT, which may act in concert to enhance mixing, dissolved gas exchange, and heat transfer in the OSBL. Future work is needed to constrain the complex interactions between waves, turbulence, and bubbles near the ocean surface and the specific manner in which coherent wave-driven motions drive spatiotemporal variability in measurements.

Acknowledgments. Luke Carberry, Jordan Snyder, and Cecily Tye assisted with field data collection. This manuscript benefited greatly from comments by Seth Zippel and two anonymous reviewers. Support for this study was provided by grants from the National Science Foundation (NSF OCE-1829952) and the Office of Naval Research (ONR N00014-20-1-2566).

Data availability statement. Data used in this study are made publicly available through the California Digital Library Dryad data repository: DOI to be included prior to publication.

Accepted for publication in *Journal of Physical Oceanography*. DOI 10.1175/JPO-D-23-0136.1.

References

Agrawal, Y., E. A. Terray, M. A. Donelan, P. A. Hwang, A. J. W. III, W. M. Drennan, K. Kahma, and S. A. Krtaigorodski, 1992: Enhanced dissipation of kinetic energy beneath surface waves. *Nature*, **359**, 219–220, https://doi.org/10.1038/359219a0.

Babanin, A. V., J. McConochie, and D. Chalikov, 2018: Winds near the surface of waves: Observations and modeling. *Journal of Physical Oceanography*, **48 (5)**, 1079–1088.

Banner, M. L., 1990: Equilibrium spectra of wind waves. *J. Phys. Oceanogr.*, **20**, 966–984.

Belcher, S. E., and Coauthors, 2012: A global perspective on langmuir turbulence in the ocean surface boundary layer. *Geophysical Research Letters*, **39 (18)**.

Chawla, A., and J. T. Kirby, 2002: Monochromatic and random wave breaking at blocking points. *Journal of Geophysical Research: Oceans*, **107 (C7)**, 4–1–4–19, https://doi.org/10.1029/2001JC001042, URL http://dx.doi.org/10.1029/2001JC001042.

Craig, P. D., and M. L. Banner, 1994: Modeling wave-enhanced turbulence in the ocean surface layer. *J. Phys. Oceanogr.*, **24**, 2546–2559.

Craik, A. D., and S. Leibovich, 1976: A rational model for langmuir circulations. *Journal of Fluid Mechanics*, **73 (3)**, 401–426.

Crosby, S. C., N. Kumar, W. C. O'Reilly, and R. T. Guza, 2019: Regional swell transformation by backward ray tracing and swan. *Journal of Atmospheric and Oceanic Technology*, **36 (2)**, 217–229, https://doi.org/10.1175/JTECH-D-18-0123.1, URL https://doi.org/10.1175/JTECH-D-18-0123.1, https://doi.org/10.1175/JTECH-D-18-0123.1.

D'Asaro, E. A., 2001: Turbulent vertical kinetic energy in the ocean mixed layer. *Journal of Physical Oceanography*, **31 (12)**, 3530–3537.

D'Asaro, E. A., J. Thomson, A. Y. Shcherbina, R. R. Harcourt, M. F. Cronin, M. A. Hemer, and B. Fox-Kemper, 2014: Quantifying upper ocean turbulence driven by surface waves. *Geophysical Research Letters*, **41**, 1–6, https://doi.org/10.1002/2013GL058193, URL http://dx.doi.org/10.1002/2013GL058193.

Accepted for publication in *Journal of Physical Oceanography*. DOI 10.1175/JPO-D-23-0136.1.

Derakhti, M., and J. T. Kirby, 2014: Bubble entrainment and liquid–bubble interaction under unsteady breaking waves. *Journal of Fluid Mechanics*, **761**, 464–506, https://doi.org/10.1017/jfm.2014.637.

Donelan, M., 1990: *Air-sea interaction*. Cambridge.

Drazen, D., W. K. Melville, and L. Lenain, 2008: Inertial scaling of dissipation in unsteady breaking waves. *J. Fluid Mech.*, **611**, 307–332.

Drennan, W. M., M. A. Donelan, E. A. Terray, and K. B. Katsaros, 1996: Oceanic turbulence dissipation measurements during SWADE. *J. Phys. Oceanog.*, **26**, 808–815.

Edson, J. B., and Coauthors, 2013: On the exchange of momentum over the open ocean. *Journal of Physical Oceanography*, **43 (8)**, 1589–1610, https://doi.org/10.1175/JPO-D-12-0173.1, URL http://dx.doi.org/10.1175/JPO-D-12-0173.1.

Fairall, C., E. Bradley, J. Hare, A. Grachev, and J. Edson, 2003: Bulk parameterization of air-sea fluxes: Updates and verification for the COARE algorithm. *J. Climate*, **16 (571-591)**.

Farmer, D., and M. Li, 1995: Patterns of bubble clouds organized by langmuir circulation. *Journal of Physical Oceanography*, **25 (6)**, 1426–1440.

Fer, I., T. M. Baumann, Z. Koenig, M. Muilwijk, and S. Tippenhauer, 2022: Upper-ocean turbulence structure and ocean-ice drag coefficient estimates using an ascending microstructure profiler during the mosaic drift. *Journal of Geophysical Research: Oceans*, **127 (9)**, e2022JC018 751.

Filipot, J.-F., F. Ardhuin, and A. V. Babanin, 2010: A unified deep-to-shallow water wave-breaking probability parameterization. *Journal of Geophysical Research: Oceans*, **115 (C4)**.

Fisher, A. W., N. J. Nidzieko, M. E. Scully, R. J. Chant, E. J. Hunter, and P. L. Mazzini, 2018a: Turbulent mixing in a far-field plume during the transition to upwelling conditions: Microstructure observations from an auv. *Geophysical Research Letters*, **45 (18)**, 9765–9773.

Fisher, A. W., L. P. Sanford, and M. E. Scully, 2018b: Wind-wave effects on estuarine turbulence: A comparison of observations and second-moment closure predictions. *Journal of Physical Oceanography*, **48 (4)**, 905–923, https://doi.org/10.1175/JPO-D-17-0133.1, URL https://doi.org/10.1175/JPO-D-17-0133.1, https://doi.org/10.1175/JPO-D-17-0133.1.

Accepted for publication in *Journal of Physical Oceanography*. DOI 10.1175/JPO-D-23-0136.1.

Fisher, A. W., L. P. Sanford, M. E. Scully, and S. E. Suttles, 2017: Surface wave effects on the translation of wind stress across the air–sea interface in a fetch-limited, coastal embayment. *Journal of Physical Oceanography*, **47 (8)**, 1921–1939, https://doi.org/10.1175/JPO-D-16-0146.1, URL https://doi.org/10.1175/JPO-D-16-0146.1, https://doi.org/10.1175/JPO-D-16-0146.1.

Gargett, A., J. Wells, A. Tejada-Martinez, and C. Grosch, 2004: Langmuir supercells: A mechanism for sediment resuspension and transport in shallow seas. *Science*, **306 (5703)**, 1925–1928.

Gargett, A. E., and J. R. Wells, 2007: Langmuir turbulence in shallow water. part 1. observations. *Journal of Fluid Mechanics*, **576**, 27–61.

Gemmrich, J., 2010: Strong turbulence in the wave crest region. *J. Phys. Oceanogr.*, **40**, 583–595, URL DOI:10.1175/2009JPO4179.1.

Gemmrich, J., 2012: Bubble-induced turbulence suppression in langmuir circulation. *Geophys. Res. Lett.*, **39 (10)**, L10 604, https://doi.org/10.1029/2012GL051691, URL http://dx.doi.org/10.1029/2012GL051691.

Gerbi, G., J. Trowbridge, E. Terray, A. J. Plueddemann, and T. Kukulka, 2009: Observations of turbulence in the ocean surface boundary layer: energetics and transport. *J. Phys. Oceanogr.*, **39**, 1077–1096.

Gerbi, G. P., J. H. Trowbridge, J. B. Edson, A. J. Plueddemann, E. A. Terray, and J. J. Fredericks, 2008: Measurements of momentum and heat transfer across the air–sea interface. *Journal of Physical Oceanography*, **38 (5)**, 1054–1072.

Goodman, L., E. R. Levine, and R. G. Lueck, 2006: On measuring the terms of the turbulent kinetic energy budget from an auv. *Journal of Atmospheric and Oceanic Technology*, **23 (7)**, 977–990.

Grant, A. L., and S. E. Belcher, 2009: Characteristics of langmuir turbulence in the ocean mixed layer. *Journal of Physical Oceanography*, **39 (8)**, 1871–1887.

Harcourt, R. R., and E. A. D'Asaro, 2008: Large-eddy simulation of Langmuir turbulence in pure wind seas. *J. Phys. Ocean.*, **38**, 1542–1563.

Accepted for publication in *Journal of Physical Oceanography*. DOI 10.1175/JPO-D-23-0136.1.

Herbers, T. H. C., P. F. Jessen, T. T. Janssen, D. B. Colbert, and J. H. MacMahan, 2012: Observing ocean surface waves with GPS tracked buoys. *J. Atmos. Ocean. Tech.*, **29**, https://doi.org/10.1175/JTECH-D-11-00128.1.

Hristov, T., and J. Ruiz-Plancarte, 2014: Dynamic Balances in a Wavy Boundary Layer. *Journal of Physical Oceanography*, **44 (12)**, 3185–3194, https://doi.org/10.1175/JPO-D-13-0209.1, URL https://doi.org/10.1175/JPO-D-13-0209.1, https://journals.ametsoc.org/jpo/article-pdf/44/12/3185/4537950/jpo-d-13-0209_1.pdf.

Husain, N. T., T. Hara, and P. P. Sullivan, 2022: Wind turbulence over misaligned surface waves and air–sea momentum flux. part ii: Waves in oblique wind. *Journal of Physical Oceanography*, **52 (1)**, 141–159.

Janssen, P. A., 1989: Wave-induced stress and the drag of air flow over sea waves. *Journal of Physical Oceanography*, **19 (6)**, 745–754.

Janssen, P. A., 1991: Quasi-linear theory of wind-wave generation applied to wave forecasting. *Journal of physical oceanography*, **21 (11)**, 1631–1642.

Janssen, P. A., 1999: On the effect of ocean waves on the kinetic energy balance and consequences for the inertial dissipation technique. *Journal of Physical Oceanography*, **29 (3)**, 530–534.

Jones, N. L., and S. G. Monismith, 2008: The influence of whitecapping waves on the vertical structure of turbulence in a shallow estuarine embayment. *Journal of Physical Oceanography*, **38 (7)**, 1563–1580.

Juszko, B. A., R. F. Marsden, and S. R. Waddell, 1995: Wind stress from wave slopes using Phillips equilibrium theory. *J. Phys. Ocean.*, **25**, 185–204.

Kenyon, K. E., 1969: Stokes drift for random gravity waves. *Journal of Geophysical Research*, **74 (28)**, 6991–6994.

Kitaigorodskii, S. A., 1983: On the theory of the equilibrium range in the spectrum of wind-generated gravity waves. *J. Phys. Oceanogr.*, **13**, 816–827.

Kukulka, T., and K. Brunner, 2015: Passive buoyant tracers in the ocean surface boundary layer: 1. influence of equilibrium wind-waves on vertical distributions. *Journal of Geophysical*

Accepted for publication in *Journal of Physical Oceanography*. DOI 10.1175/JPO-D-23-0136.1.

Research: Oceans, n/a–n/a, https://doi.org/10.1002/2014JC010487, URL http://dx.doi.org/10.1002/2014JC010487.

Kukulka, T., and R. R. Harcourt, 2017: Influence of stokes drift decay scale on langmuir turbulence. *Journal of Physical Oceanography*, **47 (7)**, 1637–1656, https://doi.org/10.1175/JPO-D-16-0244.1, URL https://doi.org/10.1175/JPO-D-16-0244.1, https://doi.org/10.1175/JPO-D-16-0244.1.

Kukulka, T., A. Plueddemann, and P. Sullivan, 2012: Nonlocal transport due to langmuir circulation in a coastal ocean. *Journal of Geophysical Research: Oceans*, **117 (C12)**.

Kukulka, T., A. J. Plueddemann, J. H. Trowbridge, and P. P. Sullivan, 2009: Significance of langmuir circulation in upper ocean mixing: Comparison of observations and simulations. *Geophysical Research Letters*, **36 (10)**.

Kukulka, T., A. J. Plueddemann, J. H. Trowbridge, and P. P. Sullivan, 2010: Rapid mixed layer deepening by the combination of langmuir and shear instabilities: A case study. *Journal of Physical Oceanography*, **40 (11)**, 2381–2400.

Kukulka, T., A. J. Plueddemann, J. H. Trowbridge, and P. P. Sullivan, 2011: The influence of crosswind tidal currents on langmuir circulation in a shallow ocean. *Journal of Geophysical Research: Oceans*, **116 (C8)**.

Kukulka, T., and F. Veron, 2019: Lagrangian investigation of wave-driven turbulence in the ocean surface boundary layer. *Journal of Physical Oceanography*, **49 (2)**, 409–429, https://doi.org/10.1175/JPO-D-18-0081.1, URL https://doi.org/10.1175/JPO-D-18-0081.1, https://doi.org/10.1175/JPO-D-18-0081.1.

Langmuir, I., 1938: Surface motion of water induced by wind. *Science*, **87 (2250)**, 119–123.

Leibovich, S., 1983: The form and dynamics of langmuir circulations. *Annual Review of Fluid Mechanics*, **15 (1)**, 391–427.

Li, M., and C. Garrett, 1997: Mixed layer deepening due to langmuir circulation. *Journal of Physical Oceanography*, **27 (1)**, 121–132.

Accepted for publication in *Journal of Physical Oceanography*. DOI 10.1175/JPO-D-23-0136.1.

Li, M., C. Garrett, and E. Skyllingstad, 2005: A regime diagram for classifying turbulent large eddies in the upper ocean. *Deep Sea Research Part I: Oceanographic Research Papers*, **52 (2)**, 259–278.

Li, M., S. Vagle, and D. M. Farmer, 2009: Large eddy simulations of upper-ocean response to a midlatitude storm and comparison with observations. *Journal of physical oceanography*, **39 (9)**, 2295–2309.

Lueck, R., 2016: Calculating the rate of dissipation of turbulent kinetic energy, rockland scientific international, victoria, canada.

Macoun, P., and R. Lueck, 2004: Modeling the spatial response of the airfoil shear probe using different sized probes. *Journal of Atmospheric and Oceanic Technology*, **21 (2)**, 284–297.

McWilliams, J. C., P. P. Sullivan, and C.-H. Moeng, 1997: Langmuir turbulence in the ocean. *Journal of Fluid Mechanics*, **334**, 1–30.

Miles, J. W., 1957: On the generation of surface waves by shear flows. *Journal of Fluid Mechanics*, **3 (2)**, 185–204.

Min, H. S., and Y. Noh, 2004: Influence of the surface heating on langmuir circulation. *Journal of physical oceanography*, **34 (12)**, 2630–2641.

Oakey, N., 1982: Determination of the rate of dissipation of turbulent energy from simultaneous temperature and velocity shear microstructure measurements. *Journal of Physical Oceanography*, **12 (3)**, 256–271.

O'Reilly, W., R. Guza, and R. Seymour, 1999: Wave prediction in the santa barbara channel. *5th California Islands Symposium, March*, Vol. 31.

Osborn, T., D. Farmer, S. Vagle, S. Thorpe, and M. Cure, 1992: Measurements of bubble plumes and turbulence from a submarine. *Atmosphere-Ocean*, **30 (3)**, 419–440.

Phillips, O. M., 1985: Spectral and statistical properties of the equilibrium range in wind-generated gravity waves. *J. Fluid Mech.*, **156**, 495–531.

Plant, B., 1982: A relationship between wind stress and wave slope. *J. Geophys. Res.*, **87**, 1961–1967.

Accepted for publication in *Journal of Physical Oceanography*. DOI 10.1175/JPO-D-23-0136.1.

Plueddemann, A. J., J. A. Smith, D. M. Farmer, R. A. Weller, W. R. Crawford, R. Pinkel, S. Vagle, and A. Gnanadesikan, 1996: Structure and variability of langmuir circulation during the surface waves processes program. *Journal of Geophysical Research: Oceans*, **101 (C2)**, 3525–3543.

Rogers, W. E., J. M. Kaihatu, L. Hsu, R. E. Jensen, J. D. Dykes, and K. T. Holland, 2007: Forecasting and hindcasting waves with the swan model in the southern california bight. *Coastal Engineering*, **54 (1)**, 1–15, https://doi.org/https://doi.org/10.1016/j.coastaleng.2006.06.011, URL https://www.sciencedirect.com/science/article/pii/S0378383906000937.

Romero, L., D. Hypolite, and J. C. McWilliams, 2020: Submesoscale current effects on surface waves. *Ocean Modelling*, 101662, https://doi.org/https://doi.org/10.1016/j.ocemod.2020.101662, URL http://www.sciencedirect.com/science/article/pii/S1463500320301645.

Scully, M. E., A. W. Fisher, S. E. Suttles, L. P. Sanford, and W. C. Boicourt, 2015: Characterization and modulation of langmuir circulation in chesapeake bay. *Journal of Physical Oceanography*, **45 (10)**, 2621–2639.

Scully, M. E., J. H. Trowbridge, and A. W. Fisher, 2016: Observations of the transfer of energy and momentum to the oceanic surface boundary layer beneath breaking waves. *Journal of Physical Oceanography*, **46 (6)**, 1823–1837, https://doi.org/10.1175/JPO-D-15-0165.1, URL http://dx.doi.org/10.1175/JPO-D-15-0165.1, http://dx.doi.org/10.1175/JPO-D-15-0165.1.

Shay, T. J., and M. Gregg, 1986: Convectively driven turbulent mixing in the upper ocean. *Journal of Physical Oceanography*, **16 (11)**, 1777–1798.

Skyllingstad, E. D., and D. W. Denbo, 1995: An ocean large-eddy simulation of langmuir circulations and convection in the surface mixed layer. *Journal of Geophysical Research: Oceans*, **100 (C5)**, 8501–8522.

Smith, J. A., 1992: Observed growth of langmuir circulation. *Journal of Geophysical Research: Oceans*, **97 (C4)**, 5651–5664.

Smith, J. A., 1996: Observations of langmuir circulation, waves, and the mixed layer. *The Air Sea Interface: Radio and Acoustic Sensing, Turbulence, and Wave Dynamics*, **613**, 622.

Smith, J. A., 1998: Evolution of langmuir circulation during a storm. *Journal of Geophysical Research: Oceans*, **103 (C6)**, 12 649–12 668.

Accepted for publication in *Journal of Physical Oceanography*. DOI 10.1175/JPO-D-23-0136.1.

Sullivan, P. P., J. C. McWilliams, and W. K. Melville, 2007: Surface gravity wave effects in the oceanic boundary layer: large-eddy simulation with vortex force and stochastic breakers. *Journal of Fluid Mechanics*, **593**, 405–452, https://doi.org/10.1017/S002211200700897X, URL http://journals.cambridge.org/article_S002211200700897X.

Sutherland, G., K. Christensen, and B. Ward, 2014: Evaluating langmuir turbulence parameterizations in the ocean surface boundary layer. *Journal of Geophysical Research: Oceans*, **119 (3)**, 1899–1910.

Sutherland, P., and W. K. Melville, 2013: Field measurements and scaling of ocean surface wave-breaking statistics. *Geophysical Research Letters*, n/a–n/a, https://doi.org/10.1002/grl.50584, URL http://dx.doi.org/10.1002/grl.50584.

Sutherland, P., and W. K. Melville, 2015: Field measurements of surface and near-surface turbulence in the presence of breaking waves. *Journal of Physical Oceanography*, **45 (4)**, 943–965, https://doi.org/10.1175/JPO-D-14-0133.1, URL http://dx.doi.org/10.1175/JPO-D-14-0133.1.

Tejada-Martinez, A., and C. Grosch, 2007: Langmuir turbulence in shallow water. part 2. large-eddy simulation. *Journal of Fluid Mechanics*, **576**, 63–108.

Terray, E., M. Donelan, Y. Agrawal, W. Drennan, K. Kahma, A. Williams, P. Hwang, and S. Kitaigorodskii, 1996: Estimates of kinetic energy dissipation under breaking waves. *J. Phys. Oceanogr.*, **26**, 792–807.

Thomson, J., E. A. D'Asaro, M. Cronin, E. Rogers, R. Harcourt, and A. Schcerbina, 2013: Waves and the equilibrium range at Ocean Weather Station P. *J. Geophys. Res.*, **118**, 1–12, URL https://agupubs.onlinelibrary.wiley.com/doi/full/10.1002/2013JC008837.

Thomson, J., M. S. Schwendeman, S. F. Zippel, S. Moghimi, J. Gemmrich, and W. E. Rogers, 2016: Wave-breaking turbulence in the ocean surface layer. *Journal of Physical Oceanography*, **46 (6)**, 1857–1870, https://doi.org/10.1175/JPO-D-15-0130.1, URL http://dx.doi.org/10.1175/JPO-D-15-0130.1, http://dx.doi.org/10.1175/JPO-D-15-0130.1.

Thorpe, S., T. Osborn, D. Farmer, and S. Vagle, 2003a: Bubble clouds and langmuir circulation: Observations and models. *Journal of Physical Oceanography*, **33 (9)**, 2013–2031.

Accepted for publication in *Journal of Physical Oceanography*. DOI 10.1175/JPO-D-23-0136.1.

Thorpe, S., T. Osborn, J. Jackson, A. Hall, and R. Lueck, 2003b: Measurements of turbulence in the upper-ocean mixing layer using autosub. *Journal of Physical Oceanography*, **33 (1)**, 122–145.

Trowbridge, J., 1992: A simple description of the deepening and structure of a stably stratified flow driven by a surface stress. *Journal of Geophysical Research: Oceans*, **97 (C10)**, 15 529–15 543.

Tseng, R.-S., and E. A. D'Asaro, 2004: Measurements of turbulent vertical kinetic energy in the ocean mixed layer from lagrangian floats. *Journal of Physical Oceanography*, **34 (9)**, 1984–1990.

Vagle, S., and D. M. Farmer, 1992: The measurement of bubble-size distributions by acoustical backscatter. *Journal of Atmospheric and Oceanic Technology*, **9 (5)**, 630–644.

Voermans, J. J., P. B. Smit, T. T. Janssen, and A. V. Babanin, 2020: Estimating wind speed and direction using wave spectra. *Journal of Geophysical Research: Oceans*, **125 (2)**, e2019JC015 717, https://doi.org/10.1029/2019JC015717, URL https://agupubs.onlinelibrary.wiley.com/doi/abs/10.1029/2019JC015717, e2019JC015717 10.1029/2019JC015717, https://agupubs.onlinelibrary.wiley.com/doi/pdf/10.1029/2019JC015717.

Wang, D. W., and P. A. Hwang, 2001: An operational method for separating wind sea and swell from ocean wave spectra. *Journal of Atmospheric and Oceanic Technology*, **18 (12)**, 2052–2062.

Weller, R. A., and J. F. Price, 1988: Langmuir circulation within the oceanic mixed layer. *Deep Sea Research Part A. Oceanographic Research Papers*, **35 (5)**, 711–747.

Zippel, S., and J. Thomson, 2017: Surface wave breaking over sheared currents: Observations from the mouth of the columbia river. *Journal of Geophysical Research: Oceans*, **122**, n/a–n/a, https://doi.org/10.1002/2016JC012498, URL http://dx.doi.org/10.1002/2016JC012498.

Zippel, S. F., T. Maksym, M. Scully, P. Sutherland, and D. Dumont, 2020: Measurements of enhanced near-surface turbulence under windrows. *Journal of Physical Oceanography*, **50 (1)**, 197–215, https://doi.org/10.1175/JPO-D-18-0265.1, URL https://doi.org/10.1175/JPO-D-18-0265.1, https://doi.org/10.1175/JPO-D-18-0265.1.

Zippel, S. F., J. Thomson, and G. Farquharson, 2018: Turbulence from breaking surface waves at a river mouth. *Journal of Physical Oceanography*, **48 (2)**, 435–453, https://doi.org/10.1175/JPO-D-17-0122.1, URL https://doi.org/10.1175/JPO-D-17-0122.1, https://doi.org/10.1175/JPO-D-17-0122.1.

Accepted for publication in *Journal of Physical Oceanography*. DOI 10.1175/JPO-D-23-0136.1.